MOTORCYCLE AERODYNAMICS

A Dissertation
SUBMITTED TO THE FACULTY OF
UNIVERSITY OF MINNESOTA
BY

Kent Underland

IN PARTIAL FULFILLMENT OF THE REQUIREMENTS
FOR THE DEGREE OF
DOCTOR OF PHILOSOPHY

Prof. Ephraim M. Sparrow

August, 2017

Contents

List of Tables

List of Figures

CHAPTER 1

INTRODUCTION

Moving vehicles present a plethora of intellectual issues related to technology. Motorcycles have unique issues that present further complexities. In particular, human interactions with the motorcycle environment are potentially an avenue for physiological injury to the rider. Those interactions involve fluid-flow-based forces that may buffet the rider in a periodic mode. The aerodynamics of motorcycles involve complicated fluid mechanic phenomena whose understanding is necessary for deducing the depth of the interactions between the rider and the motorcycle environment. The aerodynamics not only relate to human interactions, but are also relevant to the propulsion efficiency of the machine.

The focus of this thesis research is to create fundamental understanding of the external motorcycle aerodynamics and how it impacts the rider's helmet. Fluid flow involving the rider is the major focus of the research to be performed. To connect the foregoing discussion with the realities of motorcycle configurations, a photograph is displayed in Figure 1. Inspection of the figure reveals a number of aerodynamic features which are blockages and diversions from the standpoint of the oncoming flow. These blockages are concentrated on the forward portion of the motorcycle. The front fairing is primarily a cosmetic component whose presence, coupled with the windscreen, offers a substantial fluid-flow impedance and diversion. In the particular vehicle shown in the figure, the front fender is cosmetically oversized and it, too, is a flow impediment.

Figure 1.4: Side view of a typical American touring motorcycle and identification of critical components for fluid-flow blockage and diversion

The issue of rider interaction is of special interest in the proposed research. It has been examined in a cursory and uncoordinated manner in the literature. From the standpoint of human impact, it merits concerted investigation and quantification, with the intended end result being an improvement in rider wellbeing and comfort. A detailed description of specific issues relating to rider interactions with the aerodynamic environment will follow.

1.1 Causes of rider discomfort and potential injury

To assist in the discussion of rider issues, it is convenient to make reference to Figure 2. That figure shows a rider in place on the same motorcycle model that has already been displayed rider less in Figure 1.1. The figure enables the identification of the issues that relate to the impacts of the machine and the environment on rider comfort and potential injury. These impacts will be discussed in detail in the paragraphs that follow.

Figure 1.5: Photograph of a rider in place while cruising

The windscreen sheds vortices from both its lateral and upper edges. The associated buffeting is a source of both aerodynamic noise and aerodynamic forces. This situation is exacerbated with increased vehicle speed, especially due to the front fairing's role in guiding the direction of the air flow. The vortices shed from the upper edge of the windscreen propagate downstream and cause oscillating pressures on the rider's helmet. The angle of inclination and height of the windscreen along with its distance from the rider all affect the magnitude of buffeting.

Very strong aerodynamic forces can lead to vehicle instability, and extra effort is required by the rider to maintain direction. These forces can be caused by wind gusts or other vehicles on the road. The aerodynamics of the front fairing and windshield strongly influence the magnitude of those forces for which the rider must account, either by steering or adjusting the throttle. Other stability issues that may be affected by aerodynamics include wobble and weave, two modes of periodic motorcycle oscillation that can cause vehicle instability or even loss of control.

1.2 Literature

The published literature contains a number of articles that are relevant to the present investigation. The literature search was strongly focused on papers describing numerical simulation but with validating experiments. Aerodynamic forces determined by numerical simulation of the airflow passing over a motorcycle and experienced by the rider are reported in [1]. However, the results are believed to be flawed because the solution was not carried sufficiently downstream of the rider to take account of the recirculation bubble that is present in that zone. An insightful identification enumerating several categories of aerodynamic interactions experienced by a motorcycle rider is provided in [2]. However, only qualitative information in the form of streamline and vector diagrams is conveyed in the paper. A similar set of primarily qualitative results is presented in [3,4] for a special motorcycle-type designated as a Maxiscooter. The scooter lacked a fairing, however, limiting its usefulness for this research. In [5], the individual contributions from the components of a motorcycle to the overall drag force are identified. Aerodynamic forces acting on the rider's helmet were inferred from acoustic measurements in [6]. Flow visualization around a 1:7 scale model motorcycle was explored in [7]. A super-sport bike is examined in [8] using a full-scale wind tunnel and wool tufts for visualization. Consideration was given in [9] to both motorcycle aerodynamics and to the radiator heat transfer characteristics. In all of these cases, the aerodynamic results were global and lacked detail needed to characterize vortex shedding.

External aerodynamics is in major part responsible for the acoustic impacts on rider comfort and long-term dysfunction [10]. In [11-13], experiments were conducted on the interactions of vortices shed by the windscreen and the helmet of the rider. Other external aerodynamic acoustic-causing phenomena are related to the shape of the front body work (fairings) [14] and the flow separation region caused therefrom. The fluctuating wake of the motorcycle proper [15] and the wake that develops downstream of the radiator fan [16-18] are also responsible for aerodynamic acoustic vibrations. The motorcycle body as a whole may serve to amplify sound created both by external and

internal aerodynamics [19]. Special focus was directed in [20] to the sound penetration through the helmet and the resultant acoustic impact on the rider. Wind tunnel studies performed in special-purpose facilities were used in [21] to identify the acoustic issues in scale modeled motorcycle configurations.

1.3 Research Plan

The background discussion provided in the foregoing sets forth the breadth and complexity of the topic selected for this thesis research. Although numerical simulation is a viable tool to address most of the issues that were identified, necessary simplifications to the simulation model demand appropriate experimental verification. It is well established that numerical simulation is more flexible than is experiment, especially with regard to parametric variations. Another well-established practice is to seek verification only of the critical features of the simulation model. Once the critical features have been validated, the simulation is extended to encompass parametric variations. This is the approach to be adopted here.

1.3.1 Experimentation

It is contemplated that the experimental work would be performed in two separate environments. One of these is a wind tunnel specifically designed and constructed to facilitate mechanical and fluid flow measurements related to motorcycle operation. The second is an open-road test track. In general, a wind-tunnel environment differs fundamentally from an open-road environment in that the former evaluates the motorcycle in the static mode while the latter employs the motorcycle dynamically. Many of the measurements that can be made in these different venues are common, but it must be expected that differences in the extracted results will occur. This is because the motorcycles are presented with different types of oncoming flows in the two venues.

A photograph of the wind tunnel in which the experiments are to be performed is exhibited in Figure 5. The wind tunnel is operated in the suction mode. Therefore, the air that is impinging on the motorcycle and the rider is free of the swirl and backflows that

are inherent in air that is streaming downstream from axial fans. Note that the information obtained from wind tunnel studies in which the motorcycle is a stationary object is confined to aerodynamic data. The engine is not operated so that potential thermal effects do not exist.

Figure 1.6: Photograph of a wind tunnel showing a motorcycle and its rider in place

Measurements that could be made in the two venues include:

(a) Three-direction accelerometer—vibration determination and magnitude
    a. Possible instrument placement positions include: the windscreen, exterior of helmet, rider's protective garment, fairing, cylinders, exhaust pipe, mufflers, and radiator.
(b) Anemometers—measurement of velocity magnitude and direction.
    a. Instruments: hotwire / hot film, single-wire / multiple-wire, laser Doppler, vane, single-opening / multiple-opening pitot tube
    b. Placement sites: upstream of motorcycle to determine oncoming flow, just downstream of the top and side edges of the windscreen, above and to the side of the rider, between the cylinders, wake of the rider, wake of the muffler, upstream of the radiator, downstream of the radiator
(c) Static pressure taps—to determine aerodynamic forces
    a. Placement sites: in the helmet of the rider, upstream and downstream of the motorcycle.

(d) Dynamometer and load cell—integral to the test facility

The aforementioned instrumentation will produce electrical signals requiring dataloggers for their reception. The dataloggers must be capable of rapid transient response to cope with probable high-speed frequency signals. Laptop computers will be used to view the instrument outputs in real time.

The collected data will be examined and post-processed from several standpoints to facilitate diagnostic outputs. The examined data will include the relationship between the directional accelerations and the net pressure forces in their respective directions.

1.3.2 Numerical Simulation of Aerodynamics

For a synergistic approach to the aerodynamic fluid flow problem, it is appropriate to perform a numerical simulation to enhance the experimental measurements. To enable a simulation to provide results of sufficient accuracy, the solution space was extended both upstream, downstream, and laterally to the side of the motorcycle. The simulation effort was performed in two stages. At first, a two-dimensional model was created with a view toward determining the ultimate value of this simplified approach. Subsequently, a full three-dimensional model was created and implemented. A major outcome of the investigation was to identify the value of the two-dimensional approach. This is a practical issue because the implementation of a three-dimensional model requires extraordinary computer resources as well as extensive time to complete. An additional issue with respect to the simulation work is whether a steady-state approach might yield useful information or whether an unsteady model is a necessity. Once again, the implementation of the unsteady model is highly demanding of computer resources and real time for completion. The examination of this issue involved simulations based on both models.

It has been mentioned earlier that vortices shed by the windscreen are a potent source of physiological impacts on the rider. The approach here to windscreen fluid mechanics is unique with respect to prior work on the subject. In particular, the geometry of the windscreen is an important independent variable for the present investigation.

The solution domain will be extended rearward so that it encompasses the rider and continues beyond him or her. The need for such a downstream extension is that an upstream flow is actually aware of downstream happenings and adjusts to them. This approach is adopted in order to ensure that the aerodynamic forces that impinge on the rider are properly determined.

The aerodynamic interactions with the major components of the motorcycle are a necessary focus of this research. In that regard, the shape of the front fairing is a critical component because its configuration has a major effect on the magnitude and angle of attack of the wind on the windscreen. The great expanse of fairing shapes will necessitate a parametric evaluation. The shape of the front-wheel fender plays a role similar to that of the fairing. Both the fender and the fairing shapes are much more affected by stylistic issues rather than by issues of propulsion efficiency. Nevertheless, it is appropriate to quantify the effects of these components on the propulsion performance. This information has ramifications on the load on the engine and on its fuel consumption.

The need for consideration of motorcycle components situated downstream of the rider relates to the already asserted interactions of upstream phenomena with downstream fluid processes. It is well understood that models which do not extend beyond the rear fender of the motorcycle do not provide useful information about any portion of the machine or the rider.

1.3.3 Numerical Simulation Methodologies

The numerical simulation portion that has been set forth in the research plan will now be amplified. First, it is relevant to note that the external aerodynamic studies are necessarily three-dimensional, unsteady, and turbulent. Those interactions must be taken into account in order to obtain a realistic pattern of fluid flow as affected by the presence of the windscreen.

It has been noted in the expository portion of this document that upstream-situated fluids are aware of the experiences that are occurring at downstream fluid locations. This realization requires that the solution domain extend some distance, to be determined by

preliminary numerical simulations, to a sufficient length downstream of the motorcycle proper. Furthermore, the presence of the motorcycle creates a blockage that is felt by the oncoming flow, thereby demanding an upstream extension of the solution domain beyond the forward most motorcycle component. In this light, the mere determination of the proper extent of the solution domain will be a major task in itself.

The body of the motorcycle contains irregular outcroppings and indentations. Computational experiments will have to be performed to determine the extent to which the precise geometric shapes of these features have to be taken into account. Once again, preliminary numerical experiments are necessary.

Estimates of the nodal requirements to obtain numerical solutions of sufficient accuracy on a full three- dimensional model suggest that as many as 100 million nodes would be needed. That capability is uncommon but can be arranged for. If this capacity can be used, there still remains the issue of computational time to be assessed. For full accounting of the unsteady nature of the problem, the computing time might well stretch into many weeks.

Subsequent to the completion of the modeling effort, the actual execution of the numerical solutions was performed with the aid of ANSYS-CFX 17.1 software.

1.4 Concluding Remarks

The research agenda set forth in the preceding sections of this proposal is, admittedly, an ambitious undertaking. The breadth of the proposed work is, in part, influenced by the insufficiencies of previous studies reported in the published literature. That literature tends to be fragmented and too tightly focused. Here, it is recognized that there is great interaction between various components of the machine and, therefore, these components cannot be treated as entities in their right. Part of the reality of motorcycle construction is its linearity. This fact plays a major role on their inevitable interactions. It is the view of the writer that the machine must be treated as a whole.

Another strategic issue is the optimal approach to linking the numerical

simulations with the experimental work. The writer has encountered situations where there was a clear benefit in performing the simulation first and the experimentation later. This benefit occurred because the availability of the simulation results enabled optimal measurement locations to be identified. On the other hand, the availability of the wind tunnel is not continuously open. Also, the cost of using the wind tunnel is not necessarily insignificant.

CHAPTER 2

EXPERIMENTAL FACILITIES AND IMPLEMENTATION

To complement the numerical simulations, experiments were performed in two distinct venues. One of these was a wind tunnel in which the air flow was drawn into the test facility in the suction mode. The second was implemented by an instrumented motorcycle driven on an outdoor test track. These facilities are independent of each other and enable different types of data to be collected. The data from the different experiments will be compared with each other as well as with the predictions of the numerical simulations.

2.1 Test Track Experimental Facility

An aerial view of the test track experimental facility is displayed in Figure 2.1 (taken from Google Maps). As can be seen from the figure, the track is straight. Its length is 954.3 m (0.6 mi). With respect to direction, the track is approximately North-South. For the most part, the track is bordered by open space, but there is a part of the track that is bounded on the East by a clump of trees. As currently constituted, there is no weather equipment for characterizing wind speed and direction on the track itself. The weather data is recorded from Weather Underground at a location 2.5 miles southwest of the track. Recorded data include wind speed, wind direction, temperature, and barometric pressure. The track surface is smooth blacktop.

Figure 2.1 Google aerial view of the outdoor test track

The experimental procedure is initiated with a motorcycle starting from rest and accelerating to a constant speed. When the motorcycle is operated by a skilled driver, accelerating and stabilizing to a steady speed takes 17 seconds, allowing a steady velocity to be maintained for approximately eight seconds.

Test runs were performed only when the track was clean and dry for safety and to protect the measurement equipment. Testing was not permitted in winds above fifteen miles per hour in an effort to minimize wind effects. Testing was performed at temperatures ranging from 30-100 degrees Fahrenheit.

For the runs in which data were collected, the track was traversed twice, north to south and vice versa. The data collected for each direction of travel was kept separate in recognition of the probability that the wind, an unmeasured participant, would differently affect the results when the motorcycle traveled in different directions.

2.2 Wind Tunnel Experimental Facility

The other experimental facility was a subsonic wind tunnel with velocities ranging from 30 to 85 mph. Motorcycle-involved experiments were conducted for velocities between 30 and 80 mph. The wind tunnel is of the suction type with blowers situated downstream of the test section. A photograph of the test section with a motorcycle in place and with the suction fan cluster displayed in the background is presented in Figure 2.2(a). Note the fixtures which house the front and rear wheels of the machine. These fixtures are the visible portion of a dynamometer. The fan cluster consists of three axial fans, each of 72-inch diameter and with a 200 HP motor. There is a fourth fan of 42-inch diameter and 40 HP motor. Each of the fans is equipped with an individual speed controller. This fan arrangement is capable of producing a Reynolds number per foot of 800,000. Figure 2.2(b) provides an unobstructed view of the fan arrangement.

(a) (b)

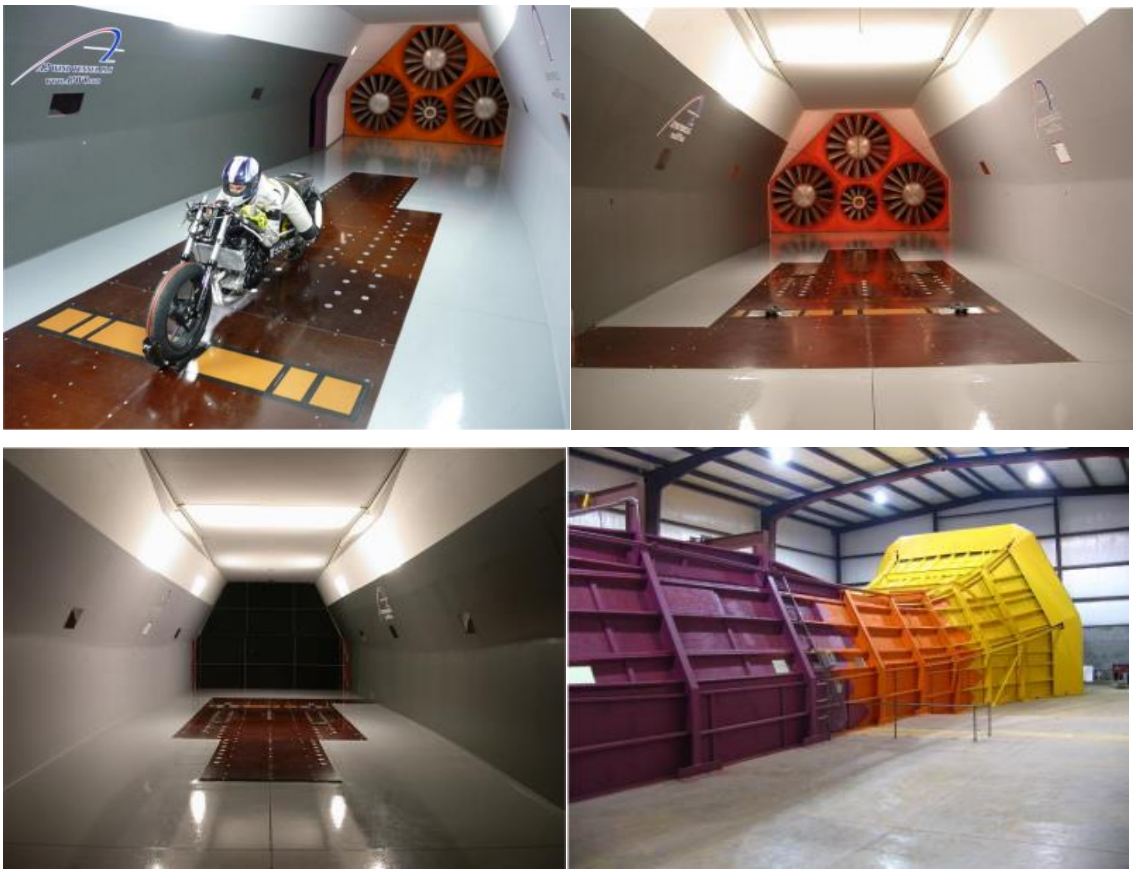

(c) (d)

Figure 2.2 Photographic views of the wind tunnel: (a) a vehicle in place in the test section, (b) unobstructed view of the bank of fans that are operated in suction, (c) upstream opening of the test section, and (d) contraction section followed by a bank of flow straighteners (not shown)

Figure 2.2(c) is an unobstructed view of the upstream opening of the test section. Flow conditioning devices are sited upstream of the opening. A view of the flow conditioning section is conveyed in Figure 2.2(d). It can be seen from the figure that air is drawn from a large space into a 6:1 contraction section. Immediately downstream of the contraction section is a honeycomb bank whose function is to serve as a flow straightener.

The wind tunnel equipment that was utilized during the experiments related primarily to flow visualization. These included: (a) a smoke machine, (b) water droplet source, (c) wool tufts, and (d) a dynamometer. The other instrumentation consisted of pressure taps and an accelerometer that will be described in more detail to follow.

All told, the wind tunnel studies were performed utilizing six different motorcycles, the distinct features of which are: (a) all of the test vehicles had varying fairings from full lowers and uppers to no fairing at all, (b) wind screen height and shape were varied systematically, (c) engine cooling systems were varied, some being water cooled and others being air cooled, (d) two different instrumented helmets were used and correlated, (e) adjustable fairing accessories such as winglets and vents, (f) presence or absence of onboard luggage carriers, and (g) presence or absence of a passenger.

Each test run in the wind tunnel consisted of 30-second constant speed intervals of low, mid, and high speed. At the end of each run, the rider recorded a perceived level of head buffeting on a scale of 1-10 with 1 being unnoticeable, and 7 or greater being considered unacceptable.

2.3 Test Equipment Used in Both Facilities

During the track-based experiments, two types of measurements were performed. One of these was pressures measured at taps deployed in the helmet of the rider. The second is accelerations measured at a site at the back of the helmet. A photograph of the helmet with installed pressure taps is conveyed in Figure 2.3.

Figure 2.3 Photograph of a motorcycle helmet displaying the locations of pressure taps

If the airflow over the helmet were to be envisioned, it may be expected that the streamlines of the flow are not parallel to the respective surface segments in which the taps are situated. This realization suggests that the pressure that is measured at the respective taps may contain a velocity pressure component that is superimposed on the static pressure. This issue will be addressed in more detail when the results of the numerical simulations are presented.

Pressure tap holes, three millimeters in diameter, were drilled to be perpendicular to the segment of the surface in which they were installed. To measure the pressure at each tap hole, a flexible plastic tube of three millimeter outer diameter and one millimeter inner diameter was inserted in the back end of the hole (internal to the helmet) and epoxied in place. The far end of each of the plastic tubes was inserted in an electronic pressure gauge (Omega PXCPC) capable of resolving 0.001-second fluctuations.

Figure 2.4 A photograph showing the position of an accelerometer affixed to the lower back face of the helmet

The accelerometer was secured to the lower edge of the back face of the helmet by means of hot glue. A photograph of this arrangement is displayed in Figure 2.4. The accelerometer reports out a displacement in three directions (X, Y, Z) and sends the signal to a data acquisition device (three channels).

A full layout of the motorcycle, rider, and test equipment within the wind tunnel is shown in Figure 2.5. The layout on the test track was similar but with the data acquisition devices located in the motorcycle's saddlebags.

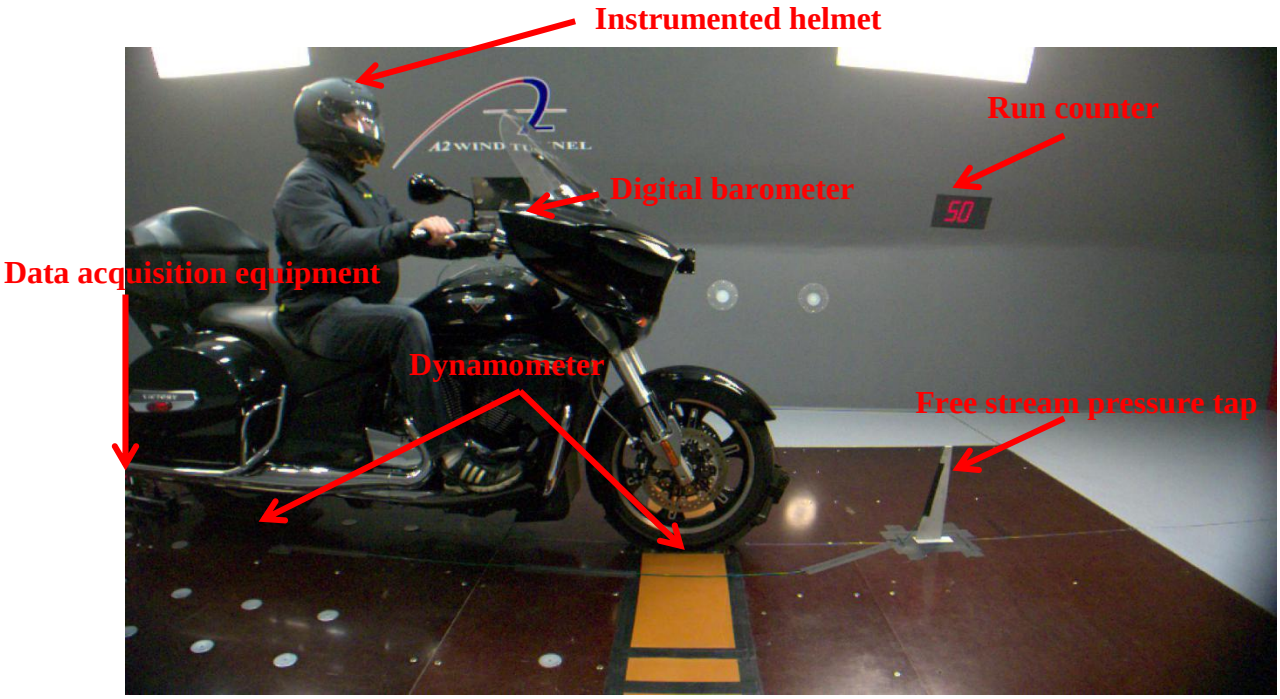

Figure 2.5 Photograph showing the full layout of the motorcycle, rider, and test equipment within the wind tunnel

2.4 Procedure

Prior to use of the wind tunnel, the tunnel operator was notified of the desired speeds for the tests. These speeds were then programmed into the wind tunnel fan controllers based on the tunnel blockage area due to each motorcycle tested.

The wind tunnel required six seconds to reach a constant low speed test section velocity from rest, another six seconds to go from low to mid speed, and an additional 16 seconds to go from mid to high speed. This left roughly 90 seconds of measurement time at each measured speed. Evaluation of the test data revealed that the 90 seconds of measurement time were sufficient to reach a steady state.

In recognition of the fact that the pressures measured at the installed taps were, in fact, gauge pressures, it was necessary to have an absolute measurement of the environmental pressure. This was accomplished by an aneroid barometer that was placed

on the dashboard of the motorcycle during each run which measured the ambient pressure at each speed and at the free stream pressure tap.

At the beginning of each run, the rider would note the barometric pressure in the tunnel with no air movement. The rider then watched for when the barometer leveled off at each wind tunnel speed, noted the ambient pressure in inches of mercury, and wrote the values down at the end of each run.

Data recording for the pressure taps and accelerometer was triggered remotely from the control room. The signal updated real time at a sample rate of 1000 Hz until the end of the test at which data acquisition was turned off.

After each run, the rider wrote down the run number, barometric pressure at each speed tested, and a subjective impression of head buffeting at each speed. The posed question asked of the motorcyclist was his overall impression of head buffeting on a ten-point scale shown in Figure 2.6 with one being no displeasure or helmet shaking and 10 being unacceptable and dangerous vibrations of the head. The use of the subjective information was supported by the knowledge that, in the real world, it is the rider's opinions that are critical.

Tolerance Scale	
0-2	Minimal/None
2-4	Noticable
4-6	Tolerable
6-8	Objectionable
8+	Unacceptable

Figure 2.6 10-point scale provided to rider for subjective evaluation of head buffeting

Wind tunnel testing showed that the speed that caused the most rider distress was 80mph, which was the maximum speed value investigated. On the test track used for alternative experiments, the motorcycle rider was able to achieve 80mph for only eight seconds. Due to this short period of time, the rider did not fill out subjective ratings for the track test.

2.5 Data Processing

As stated above, two methods were used to measure buffeting on the rider's helmet: from the readings of the three-direction accelerometer and from the pressure tap array. Both measurement environments yielded signal oscillations with a dominant frequency between 20 and 70 Hz.

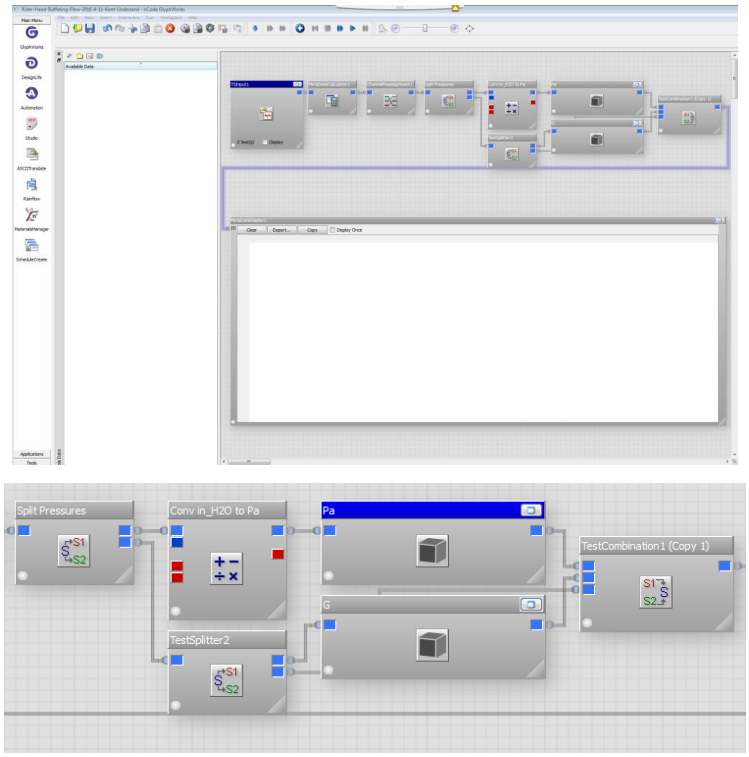

Figure 2.7 (Top) Full schematic of the data processing flow used in nCode to extract pressure and acceleration values from time series data. (Bottom) Schematic of units conversion segment, band pass filter, and one second RMS mean calculators

For the post processing of the wind tunnel data, the signals were analyzed using Glyphworks data software. First, the signals were divided into the 90-second time segments for the each fixed speed range. This was able to be done automatically by using the wind tunnel speed as a trigger to split the data series. Once the signals were split, the accelerometer signal passed through a band pass filter from 10-100Hz since this frequency range includes the majority of the relevant signals and has proven the most

impactful on rider comfort. Then, one-second RMS means were calculated from the sample data and averaged over the 90-second time frame of each speed to provide a single accelerometer value for each direction that can be compared between runs and speeds.

The pressure tap data went through a similar data processing method as the accelerometer. First, the values were filtered from 10-100Hz. Then, the RMS mean values were taken and averaged for each speed and pressure tap. It was assumed that the pressure value acted normal to the respective area segment of the helmet. The pressure tap and accelerometer results were then compiled into an Excel spreadsheet along with the subjective opinions of the riders.

In accordance with Newton's Second Law, the RMS pressure values were converted to a force using the projected helmet area in each coordinate direction, which could then be compared to the accelerations in each direction times the mass of the human head. To get the pressure force in each of the respective directions, the pressure forces had to be broken down into their X, Y, and Z components. Taking the component of pressure in each direction and area averaging each component yielded the following equations.

$$F_X = 0.08(m^2) * \frac{\frac{T_1+0.7*(T_5+T_6)}{3}+\frac{T_3+0.7*(T_9+T_{10})}{3}+T_2}{3}(Pa) \quad (2.1)$$

$$F_Y = 0.13(m^2) * \frac{0.7*(T_5+T_6+T_9+T_{10})+T_7+T_8}{6}(Pa) \quad (2.2)$$

$$F_Z = 0.16(m^2) * (\frac{T_4+0.7*(T_1+T_5+T_6+T_7+T_8)}{6})(Pa) \quad (2.3)$$

In these equations, F_n is the force in each direction in Newtons, and T_n is the respective pressure tap measurement in Pascals. The constant at the beginning of the respective equations is the projected area of the helmet in each respective direction in square meters.

The mass of an average human head is five kilograms, and the additional mass of the helmet is one kilogram, which brings the total mass of the head and helmet to six kilograms. With this knowledge and converting from g to meters per second squared yielded the following equation.

$$F_n = 6(kg) * 9.81\left(\frac{\frac{m}{s^2}}{g}\right) * a_n(g) \tag{2.4}$$

Since this equation is applicable in all three directions, F_n and a_n are used to delineate force and acceleration respectively.

Combining the foregoing equations allowed the pressure sensor and accelerometer data to be directly compared for each direction. The individual forces in each coordinate direction can be combined using Pythagorean's Theorem to yield the net non-directional force in accordance with Equation (2.5).

$$F_M = \sqrt{{F_x}^2 + {F_y}^2 + {F_z}^2} \tag{2.5}$$

When the magnitudes were calculated, the pressure forces and accelerometer measurements were found to be very close. The results of these calculations are conveyed in detail in Chapter 3.

CHAPTER 3

EXPERIMENTAL RESULTS AND COMPARISON

Experimentation using the two different facilities yielded different results due to the impact of crosswinds and the need of the rider to control the motorcycle while moving on the test track. The wind tunnel data were used as a baseline and scaling factors were developed in order to compare test track data to that collected in the wind tunnel.

3.1 Wind Tunnel Results

3.1.1 Pressure and Accelerometer Frequency Spectra

Wind tunnel testing showed that the pressure tap measurements had a strong sensitivity to the speed of the tunnel. The increases in fluctuations at roughly 100 and 200 seconds in Figure 3.1 show the response to increases in wind tunnel velocity that occur at those times. The accelerometer fluctuations increased in magnitude with speed but remained centered around zero as shown in the upper graph of Figure 3.1. The lack of offset is expected as an offset would indicate a net change in position of the rider's helmet. Pressure tap fluctuations, displayed in the lower graph of Figure 3.1, also increased in magnutude but were not centered aroud zero as for the accelerometer. The pressure fluctuated around an average that can be interpreted as the average pressure of that tap.

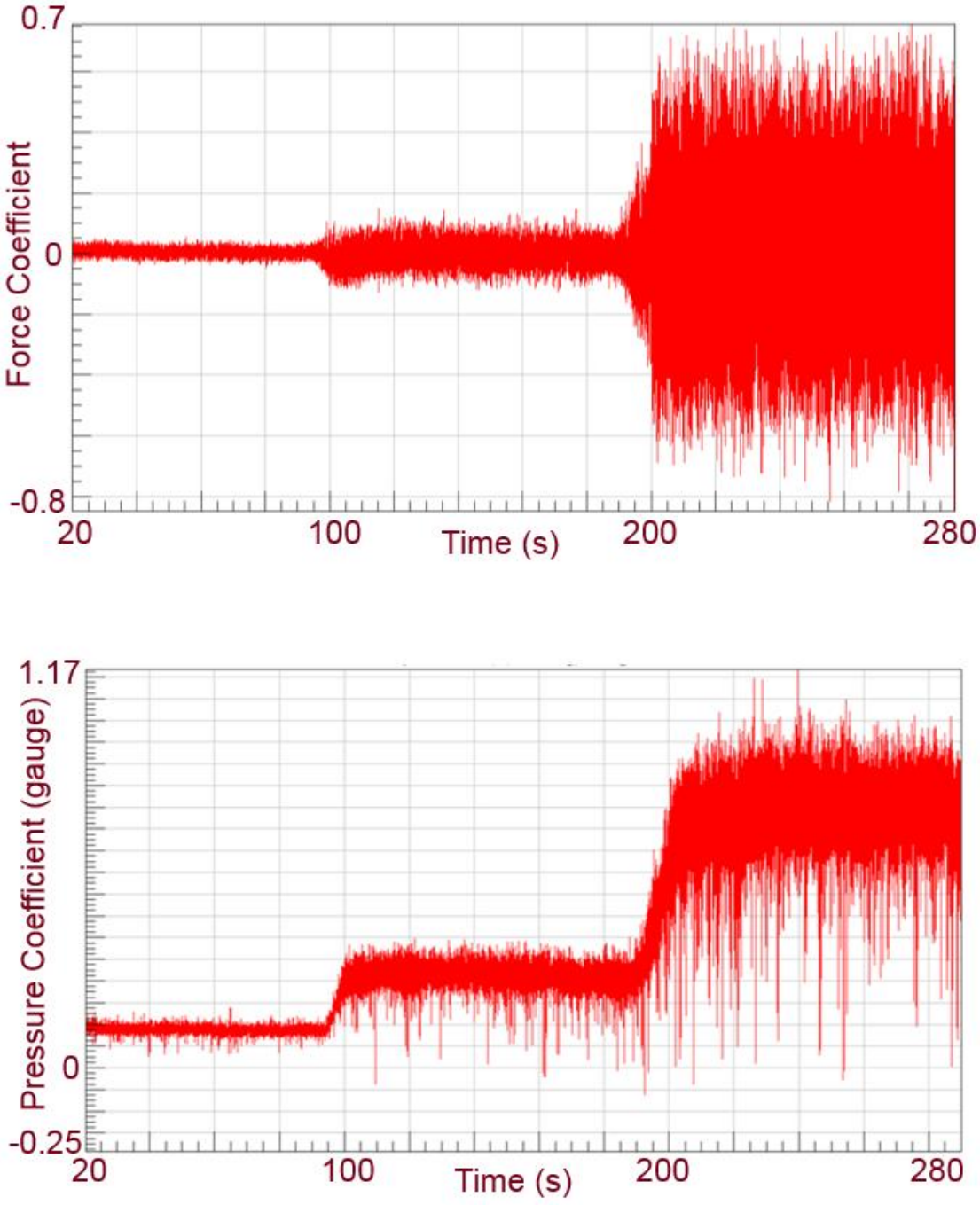

Figure 3.1 Time series graphs of x-direction accelerometer (top) and of pressure tap 1 (bottom) fluctuations at low, medium, and high speed

The frequency spectra corresponding to four different windshield heights displayed in the following figures show that the dominant frequencies of the pressure fluctuations

vary depending on the windshield position on the motorcycle. The figures display the pressure tap and accelerometer frequency spectra corrresponding to four different windshields (tall, mid, short, and none) positioned on the same motorcycle. In the accelerometer graphs, the red curve is the X or streamwise direction, blue is the side-to-side or Y direction, and green is the Z or vertical direction. The pressure curves correspond to the eleven pressure taps on the helmet and are numered in the key.

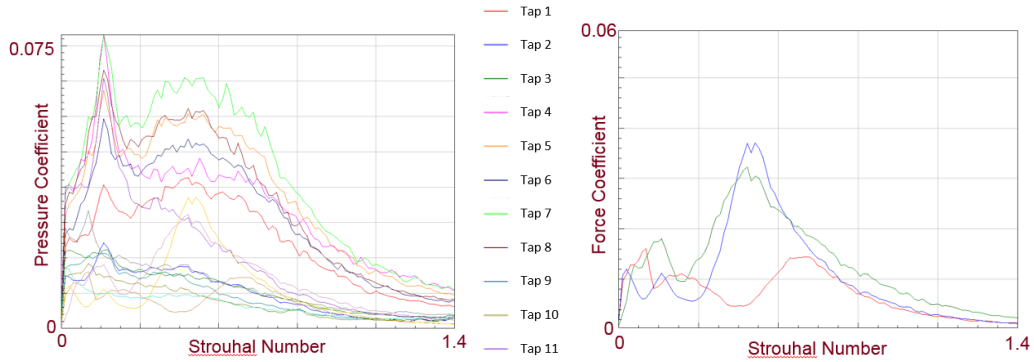

Figure 3.2 Pressure tap (Left) and accelerometer (right) frequency spectra of a tall windshield

The pressure tap spectra of the tall windshield displayed in the left graph of Figure 3.2 show an intensity spike around 11 Hz which is just barely within the human irritation range (Bruel and Kjaer). There is also a broader peak around 30 Hz. The pressure taps with the highest intensity are those on either side of the forehead (5, 6, 7, 8), which suggests that the buffeting layer is situated towards the top of the helmet as would be expected with the taller windshield. The accelerometer spectrum shows the same frequencies as high points, but the 10-Hz spike is much lower than is the 30-Hz spike. This reversal in the magnitude of the fluctuations suggests that the human/helmet system can dampen the lower frequencies seen by the pressure taps which means that they are of less importance to buffeting than the higher frequencies. Also worth noting is that the accelerometer primarily oscillates in two directions suggesting that the head is not shaking forward and backward significantly in the tall windshield case.

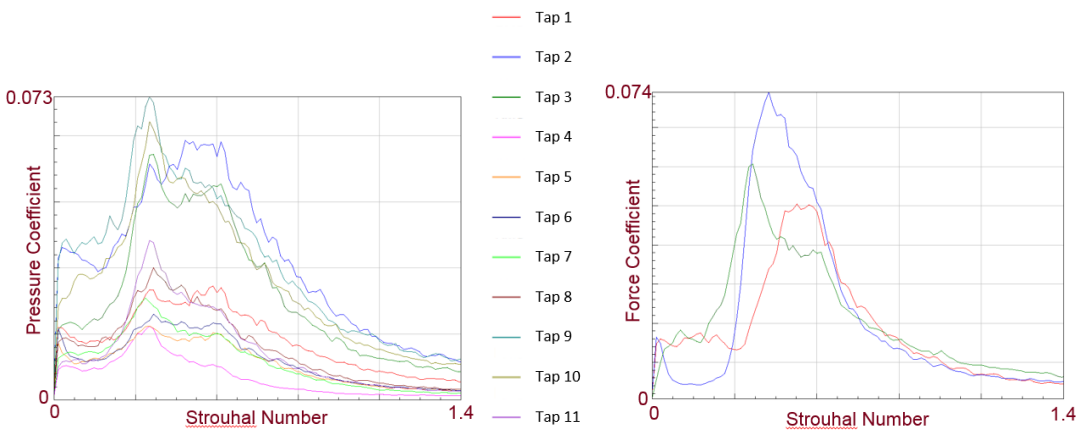

Figure 3.3 Pressure tap (left) and accelerometer (right) frequency spectra of a mid-height windshield

The results corresponding to the mid-height windscreen position are conveyed in Figure 3.3, with the pressure fluctuations displayed in the left-hand graph and the accelerometer fluctuations shown in the right-hand graph. The pressure and accelerometer fluctuations of Figure 3.3 are an order of magnitude larger than are those of Figure 3.2. In addition, the spikes in the curves have also shifted to the right. The sharp pressure spike is now centered around 25 Hz and at 30 Hz for the accelerometer. The broader shoulder for pressure is centered around 35 Hz. The dominant pressure taps have now become the taps located on the chin and face shield. This shows that the shear layer corresponding to Figure 3.3 is considerably lower than for Figure 3.2. The dominant direction of accelerometer fluctuations remains in the side-to-side direction and the peaks of each direction remain close to the same frequency. The forward and backward fluctuations now make an appearance.

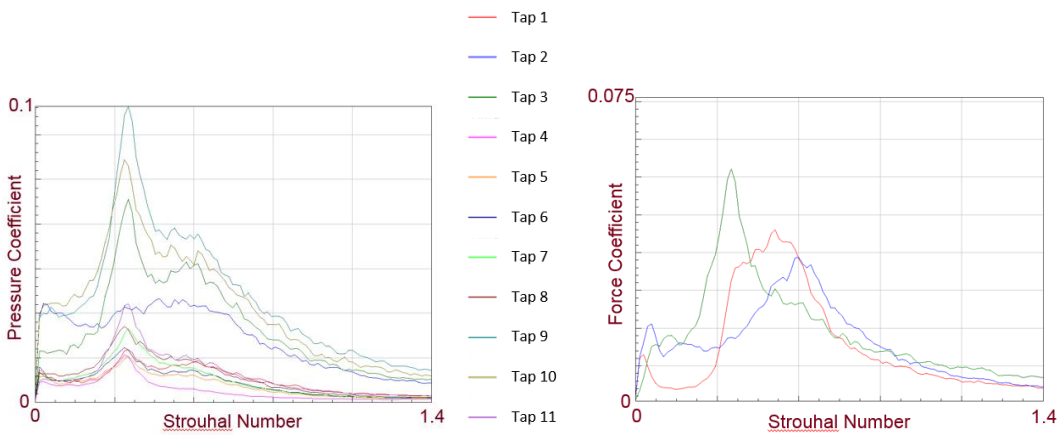

Figure 3.4 Pressure tap (left) and accelerometer (right) frequency spectra of a low windshield showing dominant locations, in this case, on the chin (taps 3, 9, and 10)

For the low windshield position, the pressure tap results in Figure 3.4 show a very strong fluctuation spike between 20 and 25 Hz that is twice as great as the fluctuations in Figure 3.3. The shoulder peak is roughly at the same power level as before, but its center has shifted to just under 40 Hz. The dominant pressure taps remain the ones located on the chin, but the tap located on the visor (tap 2) has dropped down, showing the further dropping of the shear layer to almost below the rider's helmet. The side-to-side accelerometer fluctuations have dampened significantly, but the other directions remain in the same position as for the mid-height windshield.

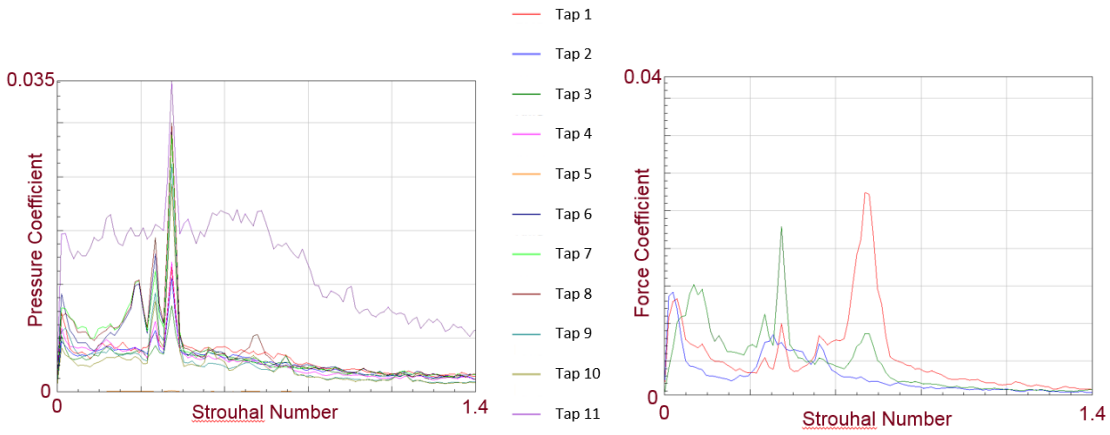

Figure 3.5 Pressure tap (left) and accelerometer (right) frequency spectra of a motorcycle with no windshield

The results for a motorcycle with no windshield (Figure 3.5) has pressure-tap fluctuation spikes centered around 22 and 27 Hz, but the magnitude is as low as that for the tall windshield, suggesting minimal buffeting. This can also be seen in the accelerometer data, where the same spikes can be seen but are dwarfed by a spike at 47 Hz.

The only pressure tap that displays consistent fluctuations across the frequency specturm up to 60 Hz for all windshiels heights is the pressure tap at the back of the helmet (shown in purple). This suggests that vortex shedding from the back of the helmet is responsible for this fluctuation and not the windshield.

After processing the data through the analysis flow described in Chapter 2, the pressure data can be seen in the color-scale table, Table 3.1. The color scale in this table goes from green being the lowest pressures to red being the highest. This table shows the sensitivity of the helmet pressure taps to different windshield types. By use of Figure 2.3, it is clear that the first bike (tall windscreen) in the table has a setup which is allowing the shear layer to impact the rider on the forehead. This can be seen by examining the table and seeing that the highest pressure fluctuations occur on the forehead pressure taps (taps 1, 4 - 8). The opposite is true in bikes two and three. In these cases, the pressure taps with the highest fluctuations are on the chin (taps 2, 3, 9, 10).

This pressure tap table can be used to show where the windshield-created vortex sheet is impinging on the helmet and provides guidance if efforts are to be made to move the sheet down or up relative to the rider's helmet. With this knowledge, the windshield can be raised or lowered to move the shear layer to the point where it no longer impinges on the helmet. This is the case for bike four. In this case, there is no fairing in front of the rider so that the helmet is entirely in the free stream. There is no buffeting effect from the motorcycle, and the only pressure fluctuations occur at the rear pressure tap. This suggests that the helmet actually induces the buffeting sensation when in the free stream.

Table 3.1 RMS-average amplitudes of the pressure fluctuations for the four motorcycles investigated. Pressure values are shown in terms of the pressure coefficient $c_P = \frac{P}{\frac{1}{2}*\rho*U^2}$

Windshield	Tap 1	Tap 2	Tap 3	Tap 4	Tap 5	Tap 6	Tap 7	Tap 8	Tap 9	Tap 10	Tap 11
Tall	0.068	0.027	0.027	0.088	0.102	0.087	0.119	0.100	0.023	0.019	0.057
Mid	0.128	0.300	0.250	0.056	0.079	0.089	0.092	0.123	0.298	0.267	0.125
Short	0.073	0.189	0.257	0.045	0.056	0.066	0.079	0.091	0.355	0.318	0.101
No	0.028	0.027	0.026	0.023	0.028	0.028	0.028	0.028	0.022	0.018	0.116

3.1.2 Force-acceleration Balance

By the use of Equations 2.1-2.5, the pressure and acceleration data from nCode were converted into comparable values of F and $m \times a$. The results from these calculations are shown in Table 3.2. In this table, as with Table 3.1, the color scale goes from low values in green to high values in red. It can be seen from the table that satisfactory agreement prevails between accelerometer measurements and pressure-based force measurement for both the x-direction and y-direction. The z-direction, however, has a somewhat weaker correlation than the other two directions. This may be due to the compressability of the human neck in the direction parallel to the the spine. Once the pressure and accelerometer magnitudes are calculated, though, the agreement between the two types of measurements is very close. The magnitudes also agreed very well with the subjective feedback of the rider.

Table 3.2 Post-processed experimental forces (P) and mass-acceleration product (A) in each direction, and the magnitude for all three directions for the four motorcycles investigated. All values are in terms of the helmet force coefficient $C_F = \frac{2*M*a}{\rho*U^2*A}$

Windshield	Ax	Px	Ay	Py	Az	Pz	Am	Pm
Tall	0.06	0.03	0.10	0.10	0.11	0.14	0.16	0.18
Mid	0.18	0.19	0.19	0.19	0.19	0.14	0.34	0.32
Short	0.16	0.16	0.11	0.19	0.18	0.10	0.26	0.27
No	0.05	0.02	0.02	0.03	0.03	0.05	0.06	0.06

To further illuminate the agreement between the pressure and acceleration measurements, Figure 3.8 plots pressure forces vs accelometer-mass products forces. The forces in the x-direction correlate the best of the directionals, followed by the y-direction, which overpredicts pressure, and the z-direction, which underpredicts pressure. The magnutude remains the best predictor, however, with very good correlation and a slope of nearly unity. This is likely due to the accelerometer not necessarily moving in the direction of the pressure fluctuations as the assumptions thus far have stated, since the head actually pivots on the neck.

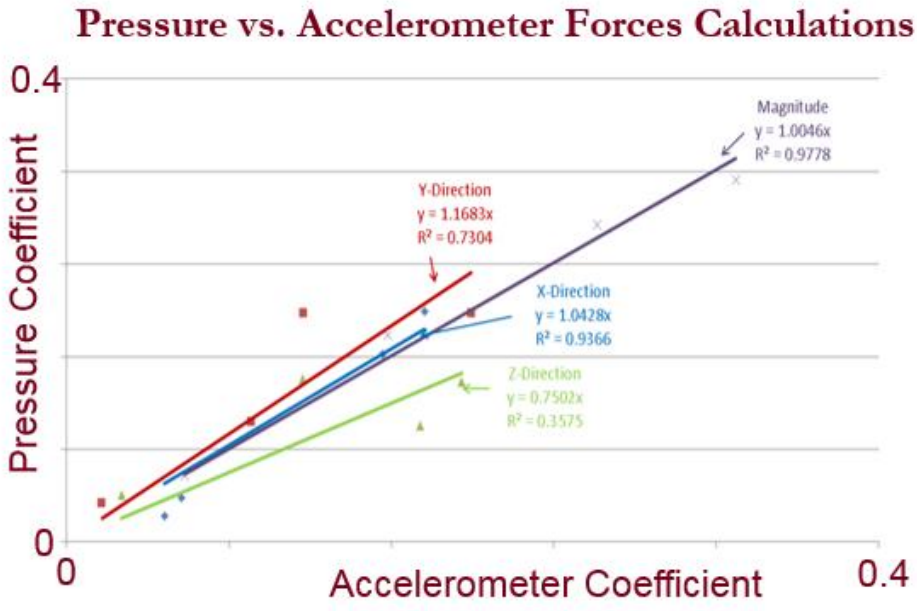

Figure 3.6 Correlation between pressure and accelerometer measurements for each direction as well for the nondirectional magnitude

3.1.3 Flow Visualization

Though the flow visualization was limited to the low speed experiments for the safety of the smoke wand operator, the visualization confirmed what the pressure tap and aceelerometer data had predicted. The upper panel of Figure 3.7, corresponding to the short windshield, shows the development of the shear layer created by the motorcycle windshield and impinging directly on the rider's head. The oscillatory nature of the flow can also be seen in the uneven top line of the smoke. Eddy formation can also be seen in the areas of smoke concentration.

Figure 3.7 Smoke visualization of the buffeting shear layer in the wind tunnel for the short (top) and tall (bottom) windshields

When the tall windshield is utilized, however, the vortex sheet flows over the top of the rider's head as seen in the lower panel of Figure 3.7. This revelation is consistent with the other measurements that predicted minimal buffeting with the tall windshield is in place but intense buffeting when the short windshield is utilized.

3.2 Test Track Results

The motorcycle with the tallest windshield was also evaluated at the outdoor test track discussed in Chapter 2 to determine impacts of crosswinds, atmospheric turbulence, and road vibrations on the measurements of the accelerometer and presssure taps. The test was performed by going back and forth along the track twice in an attempt to become directionally independent and to ensure repeatability. On the day of the test, the wind speed was four miles per hour from the South. Data collected during a typical test is displayed in Figure 3.8 where the instantaneous velocity of the motorcycle is plotted as a function of time.

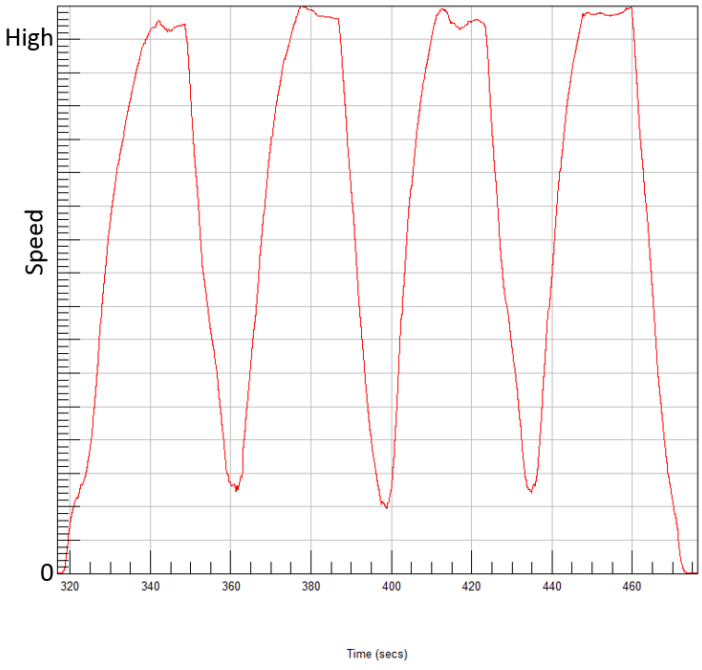

Figure 3.8 Speed data from a test-track run showing the eight-second intervals of constant high speed attained during each run

The velocity plot in Figure 3.8 shows the eight-second time durations that could be used for the test measurement. Since the crosswind speed was low, the direction of travel had minimal impact on the measurements of the pressure taps and the accelerometer. However, each eight-second interval was processed individually. Figure 3.9 compares the test-track pressure spectrum to the accelerometer spectrum. In this case though, the blue graph is the X or streamwise direction, red is the side-to-side or Y direction, and green is the Z or vertical direction.

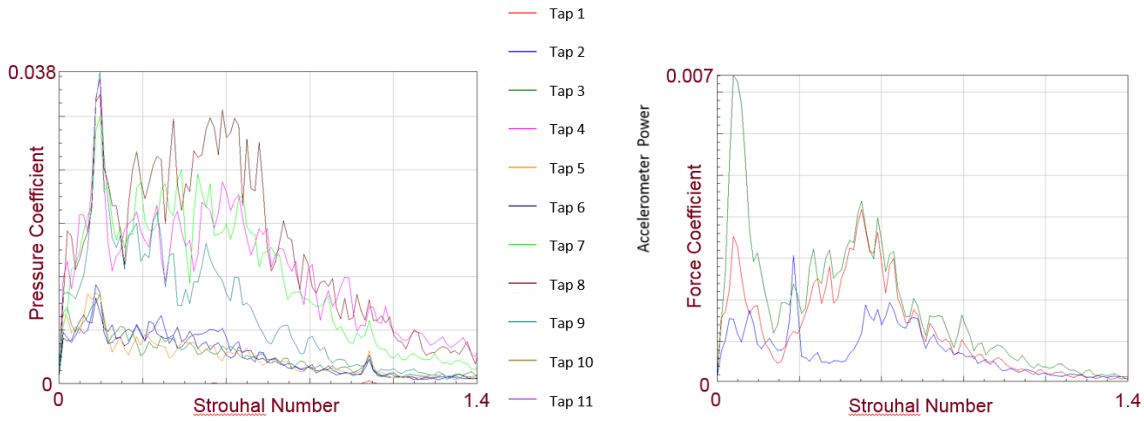

Figure 3.9 Pressure (left) and accelerometer (right) frequency spectra using the tallest windshield position on the test track

Compared to the wind tunnel measurements, Figure 3.9 shows an increase in magnitude of the pressure fluctuations by a factor of two. The pressure spike near 10 Hz that was observed in the wind tunnel is reduced relative to the broader peak but is still present. The dominant pressure taps remain the ones near the top of the helmet but now also include the pressure tap at the back of the helmet.

The accelerometer fluctuations are qualitatively similar to the wind tunnel results with a peak power level between 30 and 35 Hz. Contrary to the wind tunnel, however, is the energy spike at roughly 5 Hz which must be attributed to road inputs.

Table 3.3 shows the repeatability of the test track results. There is minimal difference between runs, and there does not appear to be a change in pressure tap

readings with vehicle direction. As with the wind tunnel, the pressure taps on the upper half of the helmet (taps 4-8) show the highest pressure fluctuations while the chin and facemask (2-3 and 9-10) are relatively low in fluctuation.

Table 3.3 RMS-average amplitudes of the pressure fluctuations for four segments of a test on the test track with the tall windshield in place. Pressure values are in terms of the pressure coefficient. Since the test was performed twice in both directions, there are four segments.

Tall WS	Tap 1	Tap 2	Tap 3	Tap 4	Tap 5	Tap 6	Tap 7	Tap 8	Tap 9	Tap 10	Tap 11
South 1	0.05	0.03	0.04	0.15	0.09	0.10	0.13	0.14	0.04	0.04	0.10
North 1	0.05	0.03	0.05	0.15	0.09	0.09	0.14	0.14	0.05	0.04	0.10
South 2	0.06	0.04	0.04	0.15	0.09	0.09	0.14	0.14	0.04	0.04	0.12
North 2	0.06	0.04	0.05	0.16	0.10	0.10	0.14	0.16	0.04	0.04	0.11

Table 3.4 shows the post-processed forces from both the accelerometer and pressure tap readings. The pressure and accelerometer readings agree very well in each direction and in magnitude. The repeatability of the accelerometer measurements can also be seen in this table. This level of agreement provides further testimony as to the lack of a crosswind during the time of the tests.

Table 3.4 Post-processed pressure and accelerometer measurements in each direction and the magnitude of all three directions for runs on the test track with the tall windshield in place. All values are in terms of the force coefficient

Windshield	Ax	Px	Ay	Py	Az	Pz	Am	Pm
South 1	0.064	0.048	0.128	0.128	0.192	0.160	0.223	0.207
North 1	0.064	0.048	0.128	0.128	0.192	0.176	0.239	0.223
South 2	0.064	0.048	0.128	0.128	0.192	0.176	0.239	0.223
North 2	0.064	0.048	0.144	0.144	0.192	0.192	0.255	0.239

3.3 Comparison of Wind Tunnel and Test Track Results

When compared to the pressure tap measurements made in the wind tunnel, the measurements made on the test track had significantly higher fluctuations in some tap locations. Qualitatively, though, the results are similar in that both predict the presence of a vortex layer spawned by the windshield and impinging on the upper portion of the helmet for the tall windscreen. This is seen in Table 3.5 as reflected in the high RMS

values of pressure in taps four through eight. One interesting difference is the increase in pressure RMS levels on pressure tap 11 (the back of the helmet).

Table 3.5 Comparison of pressure tap measurements from the wind tunnel and test track. Pressure values are in terms of the pressure coefficient

Tall WS	Tap 1	Tap 2	Tap 3	Tap 4	Tap 5	Tap 6	Tap 7	Tap 8	Tap 9	Tap 10	Tap 11
Wind Tunnel	0.068	0.027	0.027	0.088	0.102	0.087	0.119	0.100	0.023	0.019	0.057
Test Track	0.056	0.036	0.046	0.155	0.091	0.096	0.137	0.144	0.043	0.041	0.107

Though the pressure taps readings differ in a few locations when comparing the wind tunnel to the test track, the agreement improves somewhat when looking at the post-processed pressure and accelerometer values in Table 3.6. The measurements in the x- and y-directions are almost identical. The z-direction measurements are slightly off but still very close.

Table 3.6 Comparison of post-processed wind tunnel and test track data. All values are in therms of the force coefficient

Windshield	Ax	Px	Ay	Py	Az	Pz	Am	Pm
Wind Tunnel	0.064	0.032	0.096	0.096	0.112	0.144	0.160	0.176
Test Track	0.064	0.048	0.128	0.128	0.192	0.176	0.239	0.223

The higher test track RMS pressures on the top and back of the helmet suggest that the shear layer moved down relative to the rider's helmet. This could be due to multiple factors including a change of rider posture due to natural riding conditions or atmospheric turbulence due to the surrounding geography.

When comparing to what a rider will actually experience on a highway, the test track is likely the more realistic case. This is due to the much more similar environments between the test track and the highway. The advantage of the wind tunnel is that it is more repeatable in the sense that there may be days on the test track when the crosswind obscures the data. Also, the wind tunnel avoids the elements such as cold and rain, which would impact the rider's opinion of buffeting and could harm the measurement equipment. Another major benefit of the wind tunnel, though, is that it is easier to model in CFD and provides a better comparison for validating computational modeling.

CHAPTER 4

NUMICAL SIMULATION MODELING AND IMPLEMENTATION

The investigation performed here is a synergistic activity involving both numerical simulation and experimentation. This chapter is devoted to providing an in-depth exposition of both the simulation models that were developed and the numerical techniques that were employed to exercise those models.

4.1 Physical Models for Numerical Simulation

Three models were used to understand the flow field about a stationary motorcycle situated in uniform oncoming freestream. This is the physical situation that was encountered in the experiments performed in the wind tunnel. Particular focus is directed to the neighborhood of the rider's head to complement and compare with experimental data set forth elsewhere in this thesis. The numerical complexity of this problem has prompted a three-step approach. The starting point is a two-dimensional model, which has enormous computational advantages but is unable to model reality with precision. The more realistic model is three-dimensional, but requires very extensive computer resources. As a compromise between computational convenience and ultimate accuracy, a partial three-dimensional model was devised and implemented to be described shortly. Lastly, with the two-dimensional and full three-dimensional models, a full transient model was performed to validate the steady-state results.

4.1.1 Two-dimensional model

The starting point is a two-dimensional model based on cutting a vertical plane through the longitudinal axis of the motorcycle as shown schematically in red outline in Figure 4.1. The plane has been filled with a transparent color for easy identification. It is worthy of note that only that part of the plane that contains fluid constitutes the solution

domain. Any solid surfaces that are contained within the plane are regarded as no-slip and impermeable surfaces in accord with the fundamental laws of flow mechanics. This model is readily implemented numerically and yields solutions in relatively short periods of time. It is this capability that makes the model attractive.

The solution domain extends forward of the leading edge of the machine by two motorcycle lengths, and the rearward extension is five such lengths. To model the situation in which the motorcycle was positioned in a wind tunnel, the upper edge of the solution domain was chosen to be two heights of the motorcycle.

Figure 4.1 Schematic diagram depicting a vertical plane which includes the longitudinal axis of the motorcycle. The shaded volume is the two-dimensional solution domain

To properly describe the physical model, it is appropriate to state the boundary conditions. At the forward edge of the solution domain, a uniform velocity is imposed along with a uniform value of turbulence intensity of 5%. At the downstream edge of the domain, very weak boundary conditions are specified in recognition of the fact that the true conditions are not really known. Specifically, the streamwise second derivatives of all the velocity components are taken to be zero, and the average pressure is specified. If gauge pressures are used, then the gauge pressure is set to zero.

At the top of the solution domain, it is envisioned that that location corresponds to the roof of a wind tunnel. Since the roof is a solid surface, it is appropriate that that surface be no-slip and impermeable. Those parts of the bottom of the solution domain that do not interact with a solid surface have been specified as free-slip boundaries. A free-slip boundary does not permit fluid to cross it but requires that immediately adjacent fluid be perfectly parallel to the boundary.

4.1.2 Partial three-dimensional model

The next model extends the solution domain of Figure 4.1 to three dimensions, but does not encompass the entirety of the motorcycle or the rider. To define the partial three-dimensional domain, envision that the red boundary displayed in Figure 4.1 is widened so that its total width is equal to five motorcycle widths. This configuration encompasses the motorcycle itself plus two widths to either side. The boundary conditions on the extended solution domain remain the same as those described in the foregoing. For the newly created side boundaries of the domain, it is envisioned that these constitute wind tunnel walls and are, therefore, no-slip and impermeable.

4.1.3 Full three-dimensional model

The final model contains the entire motorcycle from the ground up to the edges of the previous domains. The boundary conditions remain the same as in the previous partial three-dimensional model with the exception being the newly present ground plane. To simulate the wind tunnel condition, the ground boundary is considered no-slip and impermeable.

4.2 Governing Equations

The starting point of the turbulent flow simulations is the momentum conservation equation for three–dimensional, incompressible, constant-property, and unsteady flow. This equation, expressed in Cartesian-tensor form, is conveyed by Eqs. (1). These equations are commonly known as the RANS equations. The quantity μ_{turb} is the turbulent viscosity, which represents the Reynolds stresses. In the RANS formulation,

$$\rho\frac{\partial u_j}{\partial t}+\rho\left(u_i\frac{\partial u_j}{\partial x_i}\right)=-\frac{\partial p}{\partial x_j}+\frac{\partial}{\partial x_i}\left((\mu+\mu_{turb})\frac{\partial u_j}{\partial x_i}\right)\quad j=1,2,3\quad i=1,2,3 \tag{1}$$

turbulence isotropy is intrinsic. These equations are supplemented by the equation of continuity.

$$\frac{\partial u_i}{\partial x_i}=0 \tag{2}$$

The selection of the **SST** *k*-ω turbulence model [22] for application here is based on a substantial literature. In this regard, reference may be made to [23-25] for successful applications of the SST *k*-ω model to bends and for separated flows [26]. In addition, our laboratory personal have demonstrated the validity of the model for duct flows [27] and for flow through perforated plates [28]. Most recently, they have employed the comprehensive swirl-based data of [29] as input to demonstrating the competence of the SST *k*-ω model for swirling flow and for flows with both laminar and turbulent portions [30].

The equations of the SST model are partial differential equations for the turbulence kinetic energy κ and the turbulent eddy frequency ω. They are

$$\frac{\partial(\rho\kappa)}{\partial t}+\frac{\partial(\rho u_i\kappa)}{\partial x_i}=P_\kappa-\beta_1\rho\kappa\omega+\frac{\partial}{\partial x_i}\left[\left(\mu+\frac{\mu_{turb}}{\sigma_\kappa}\right)\frac{\partial\kappa}{\partial x_i}\right] \tag{3}$$

$$\frac{\partial(\rho\omega)}{\partial t}+\frac{\partial(\rho u_i\omega)}{\partial x_i}=A\rho S^2-\beta_2\rho\omega^2+\frac{\partial}{\partial x_i}\left[\left(\mu+\frac{\mu_{turb}}{\sigma_\omega}\right)\frac{\partial\omega}{\partial x_i}\right]+2(1-F_1)\rho\frac{1}{\sigma_{\omega2}\omega}\frac{\partial\kappa}{\partial x_i}\frac{\partial\omega}{\partial x_i} \tag{4}$$

The solution of Eqs. (3) and (4) yields the values of κ and ω, which give the turbulent viscosity μ_{turb} from

$$\mu_{turb} = \frac{\rho k}{\max(\omega, SF_2)} \tag{5}$$

Quantities relevant to Eqs. (3) to (5)

A	model constant
F_1, F_2	blending functions in the SST model
P_k	production term for the turbulent kinetic energy
S	absolute value of the shear strain rate
u_i	local velocity
x_i	tensor coordinate direction
α	SST model constant
β_1, β_2	SST model constants
ω	turbulent eddy frequency
κ	turbulence kinetic energy
μ	molecular viscosity
μ_{turb}	turbulent viscosity
σ	Prandtl-number-like diffusion coefficient
ρ	fluid density

The foregoing partial differential equations were discretized by means of the finite volume technique. This technique is embedded in the ANSYS CFX 17.1 software which was used for the numerical simulations.

4.3 Numerical Simulations

The discretization of the governing partial differential equations requires the positioning of nodes and the selection of the time step for the transient portion of the solution. A node is a point in space at which the solution is obtained. The placement of the nodes is an operation called meshing. For problems of the complexity of those encountered here, it is absolutely necessary that node numbers in the millions be used. For example, in the three-dimensional model described in the foregoing, approximately 15 million nodes were used. On the other hand, for the two-dimensional model, approximately 600,000 nodes were deemed sufficient.

Both steady-state and transient operating conditions were used to investigate the flow phenomena around the motorcycle. When the steady-state model was set up and executed for numerical simulation, the results continued to display iteration-by-iteration variations without hint of convergence. These variations are reported as such. They also were used to provide the initial conditions required to perform a transient numerical solution. The transient model captures the fluctuating nature of the flow over the windshield and around the fairing, which can be used to predict buffeting more directly.

The choice of a time step in the case of the transient model is somewhat related to the number of nodes. The closer the spatial proximity of nodes, the larger is the permissible time step. For the computations performed here, an acceptable time step was found to be 0.002 seconds. When a transient problem is being solved, the solution technique involves a number of iterative steps (loops) between two consecutive times. It was found sufficient to use 10 such inner-loop iterations. The total simulated time for each run was one second which allowed a total of 500 outer loop time steps. This provided a sufficient time window to characterize the time varying nature of the flow.

To judge convergence of the respective steady-state and transient solutions, two approaches were used. One of these, standard in numerical solution methodology, is to monitor the RMS residuals for each of the governing equations. A residual is a left-over when each equation is evaluated using the most current information for the velocities and

pressure. A second means of judging convergence was to select a particular metric to be followed during the successive steps of the numerical work. In particular, the forces in each of the three coordinate directions exerted by the fluid on the helmet were evaluated at each step and monitored. The two means of judging convergence were mutually supportive.

4.4 Sought-for-Results

The simulation equations that were set forth in Eqs. (1)-(5) were solved with the view to determining many features of the velocity and pressure fields. The results that will be obtained by post-processing include:

(a) The pressure field at all points in the solution domain, with special focus on the pressures exerted on the helmet
(b) The total drag on the motorcycle and the rider as a function of the motorcycle speed
(c) Frequency content of the transient solutions
(d) The velocity field at all points in the solution domain, with emphasis on the area directly around the rider

All of these results are to be compared with the experimental data obtained in the wind tunnel tests and, to a lesser extent, with the data collected on the test track.

CHAPTER 5

NUMERICAL MODEL RESULTS

As was set forth in earlier chapters, several models were implemented by means of numerical simulation. These include: (a) two-dimensional in the steady state, (b) two-dimensional in the unsteady state, (c) three-dimensional steady confined to a limited geometry (partial three-dimensional), (d) three-dimensional in the steady state for the complete motorcycle geometry, and (e) three-dimensional in the unsteady state for the complete motorcycle geometry. The results of each model provide increasing fidelity of the predicted flow phenomena surrounding the motorcycle rider to reality. The steady-state models were able to capture the presence of a shear layer situated between the free stream and the area immediately behind the windshield and the *de facto* forces acting on the rider. The transient models were able to define the time-varying vortex shedding spawned by the windshield and fairing. The model of the complete motorcycle provided the transient pressure variation at multiple helmet locations that could then be processed to produce a pressure fluctuation frequency and amplitude.

5.1 Two-Dimensional Model

5.1.1 Steady-State Results

The two-dimensional, steady-state model provided limited definition of the flow around the rider but identified the shear layer spawned by the windshield. An example of the steady-state velocity contours can be seen in Figure 5.1.

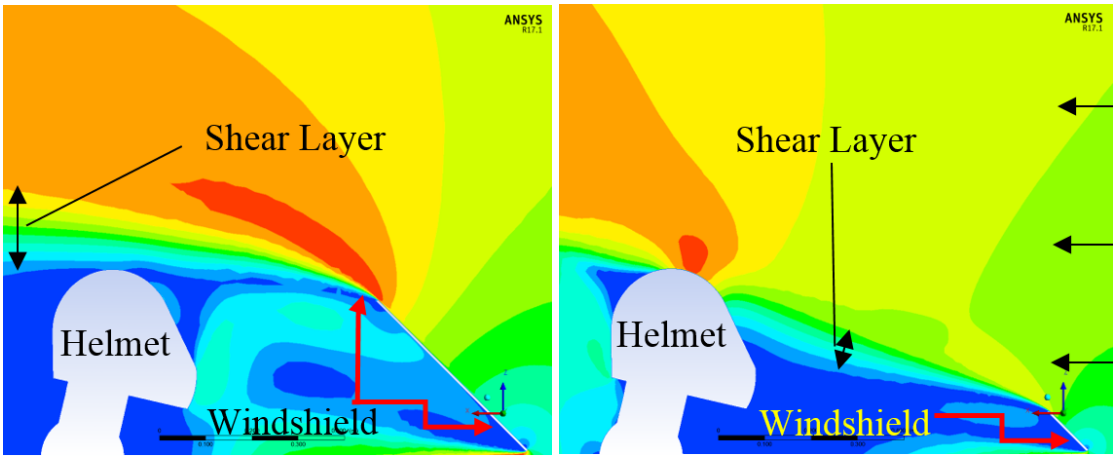

Figure 5.1 Steady-state velocity contours corresponding to the two-dimensional tall (left) and short (right) windshields showing the differing flow characteristics about the rider's helmet

Due to the larger blockage of the tall windshield, the airstream is more accelerated coming off of the windshield, but it almost completely misses the rider's helmet. This suggests that buffeting would be minimal with the tall windshield. The short windshield, on the other hand, produces a smaller airspeed coming off of the windshield, but the shear layer directly impinges on the rider's head. This suggests that head buffeting would be a concern with this windshield. Another interesting characteristic of the short windshield model is that the maximum velocity is located above and behind the rider's helmet, as seen in Figure 5.2, which displays streamlines This is likely due to the nature of the two-dimensional model and a strong recirculation zone behind the rider's helmet.

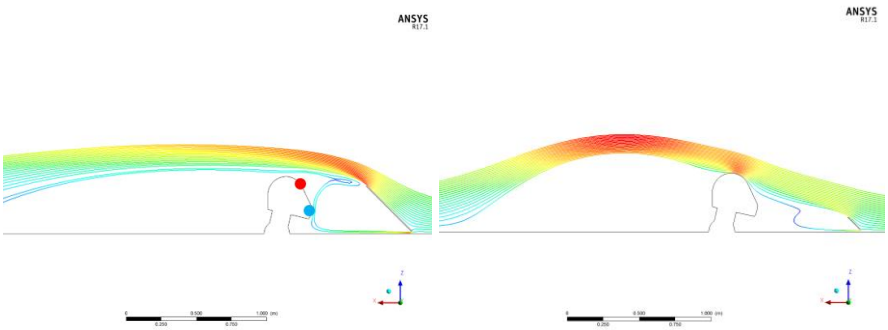

Figure 5.2 Velocity streamlines over a two-dimensional tall (left) and short (right) windshield. The dots indicate the locations of chin and forehead pressure taps

5.1.2 True Transient Results

Pressure taps, located at positions one and three (respectively, the blue and red dots in Figure 5.2), were monitored to capture the transient pressure fluctuations on the helmet. The curves in Figure 5.3 show how pressure fluctuations vary with windshield height.

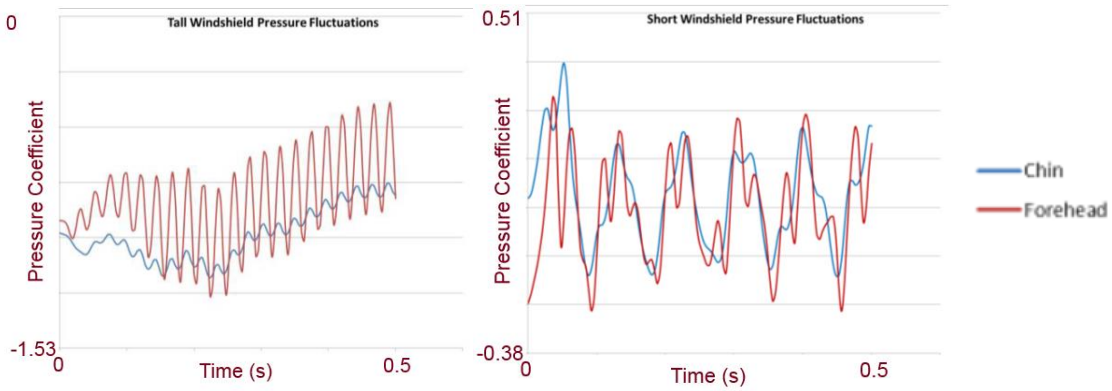

Figure 5.3 Pressure vs time corresponding to the two-dimensional tall (left) and short (right) windshields

The tall windshield results display a very high frequency fluctuation while the short windshield shows a much lower frequency with a more chaotic variation. While the tall windshield pressure levels are negative at both taps, the short windshield pressure taps oscillate between positive and negative. The latter outcome indicates that the shear

layer is actually flipping back and forth over the helmet. Lastly, the amplitude of the pressure fluctuations at the two taps appear to be similar in the case of the short windshield, but the tall windshield creates a stark contrast in amplitude between the forehead tap and the chin tap. The lower amplitude at the chin area suggests that the chin is relatively protected from the turbulent shear layer with the tall windshield in place. Further observation of Figure 5.3 shows that the total swing of the pressure (maximum-to-minimum) is about the same for the measurements corresponding to the short windshield and tall windshields.

5.2 Partial Three-Dimensional Model in the Steady State

The next model to be utilized in the simulation work is defined as a partial three-dimensional model. That model includes the lateral extension of the solution domain, but omits the lower part of the domain that is beneath the windshield.

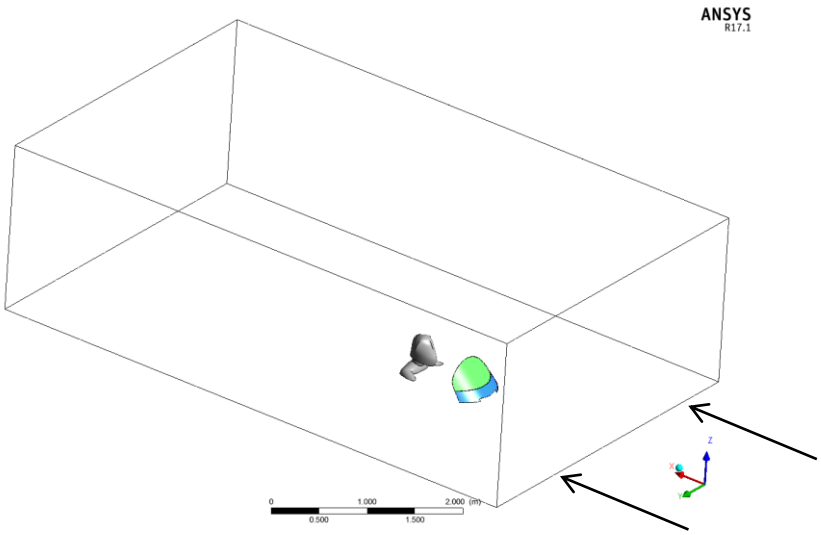

Figure 5.4: Control volume for partial 3-D model with two windshield heights and rider above the shoulders

The addition of the third dimension to the windshield model provided a means for understanding of the flow around the sides of the windshield and the rider's helmet.

Figure 5.4 shows the expansion of the fluid volume to the left and right of the rider. The two windshields modeled are shown in green (tall) and blue (short).

The streamlines in Figure 5.5 show the relationship between the rider and the windscreen at heights corresponding to the top edge of the short windscreen (part (a)) and 100 millimeters above it (part (b)). The streamlines in this figure are initialized on a line that runs across the width of the windshield located just ahead of the windshield. The importance of the interaction between the helmet and windshield can be seen by comparing (a) and (b) in how the streamlines dip down below the rider's helmet before rising again over his shoulders with the short windshield (b).

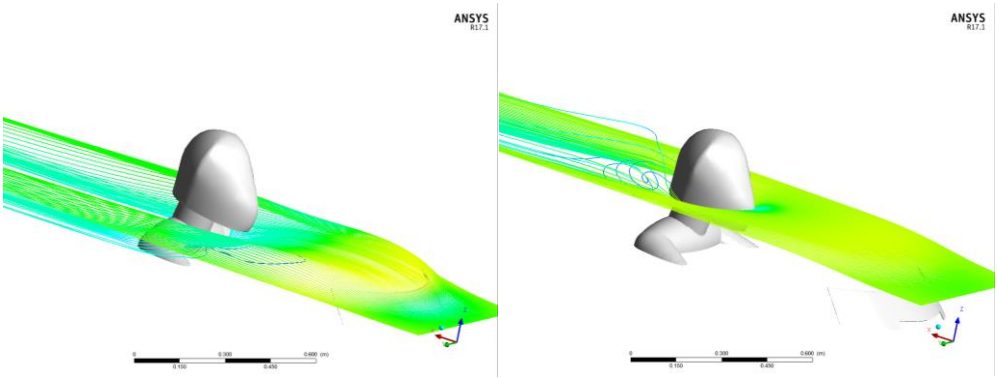

(a) (b)

Figure 5.5 Velocity streamlines at the height of the short windshield (left) and 100 mm above (right)

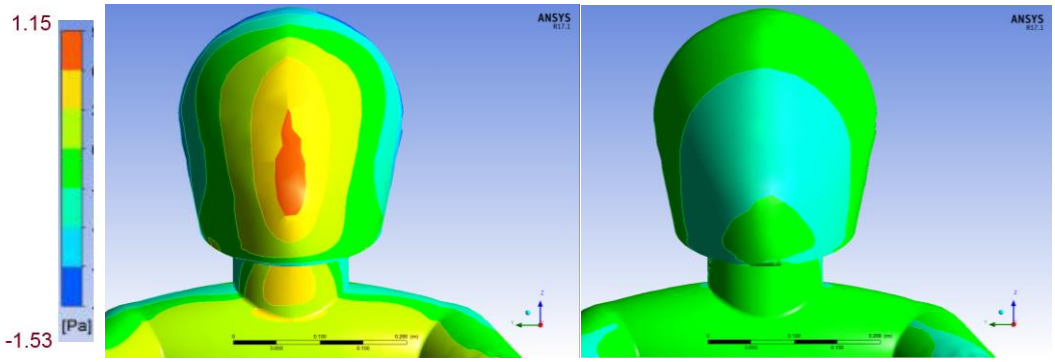

Figure 5.6 Pressure contours on the helmet corresponding to the short (left) and tall (right) windshields. The scale is the same in both images

The pressure contours corresponding to the two windshield are conveyed in Figure 5.6, respectively in the left- and right-hand graphs for the short and tall windshields. They show a peak in pressure at the front and center of the helmet while the low pressure areas are on the sides, indicating that the head is in the free stream of air. The tall windshield pressure contour is mostly uniform, which shows that most of the air goes over the rider's head without interacting with the helmet.

Comparing results for the two-dimensional and partial three-dimensional models in Figure 5.7, it can be seen that the third dimension has an impact on the height of the shear layer in steady state. For the short windshield, the shear layers of the respective two-dimensional and three-dimensional models have very different characteristics, actually dipping under the rider's helmet in the partial three-dimensional case and impinging near the forehead in the two-dimensional model. The tall windshield cases are more similar, but the shear layer is lower in the three-dimensional case. There is likely no impingement of the shear layer on the helmet in the tall-windshield, dimensional case, but the three-dimensional case shows some impingement.

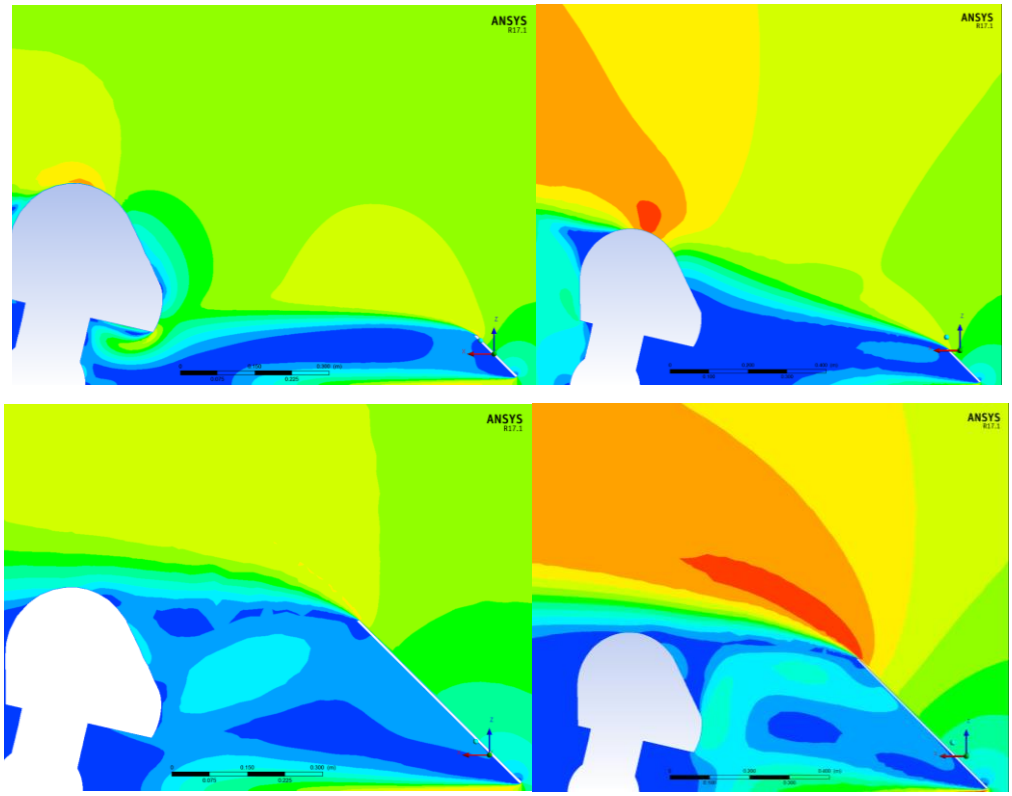

Figure 5.7 Velocity contours of the short (top) and tall (bottom) windscreens in both 2-D (right) and partial 3-D (left) models

Adding the third dimension also greatly reduced the maximum velocity over the rider's head, since lateral motion can occur in a three-dimensional model. This is due to the presence of additional free stream space on either side of the helmet and windshield. With this space on either side of the helmet and windshield, the air does not necessarily need to go over the helmet and windshield but can, instead, go around the sides of the blockages.

Comparing the tall to the short windshield in these models, the latter clearly creates higher velocities at the rider's helmet. This is clear in both models. Comparison of the relative calm at the rider's helmet shows that the tall windshield is clearly a more comfortable solution for the rider and should provide much less buffeting.

5.3 Full Three-Dimensional Model

5.3.1 Steady State

The full three-dimensional model includes the rest of the motorcycle geometry. This work revealed the importance of a more comprehensive geometric model for determining the windshield performance. The full model included the entire motorcycle from the road plane up to two heights of the vehicle above it, two vehicle widths to either side, two vehicle lengths upstream, and five vehicle lengths downstream. In this model, three motorcycle configurations were tested, a short windshield, a mid-height windshield, and a tall windshield. In order to better correlate to the test results, the instrumented buffeting helmet was scanned into the model with the pressure tap locations marked. This provided an opportunity to directly compare the analytical model to test.

Instantaneous steady-state velocity contours for all three windshield heights are shown in Figure 5.8. The shear layer of the short windshield hits the rider at the visor while the mid-height windshield impinges on the forehead. The tall windshield pushes the shear layer completely over the rider's head. This is qualitatively similar to the partial three-dimensional and the two-dimensional results. The inclusion of the rest of the motorcycle in the model shows the change in flow characteristics below the shear layer as well. There is now chaotic flow in the pocket below the shear layer.

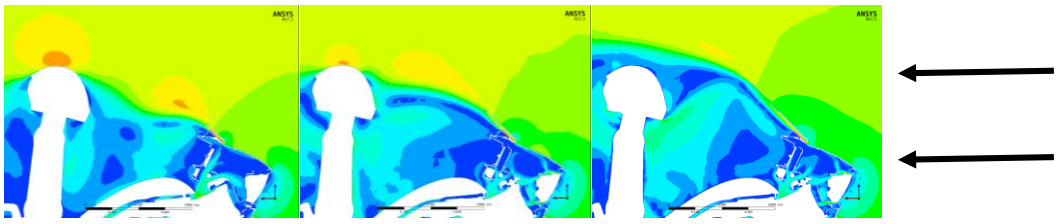

Figure 5.8 Vertical centerplane velocity contours of short (left), mid (center), and tall (right) windshields.

Looking back and comparing to the results of the partial three-dimensional model and of the two-dimensional model,it is seen that the additional geometry of the full three-dimensional model clearly impacts the shear layer height (Figure 5.9). The additional geometry of the motorcycle places the shear layer of the short windshield at the visor height of the helmet, about half way between what was predicted by the two-dimensional and three-dimensional models. The full three-dimensional model also reveals a larger amount of chaotic air below the shear layer which is likely coming up from the lower portion of the motorcycle.

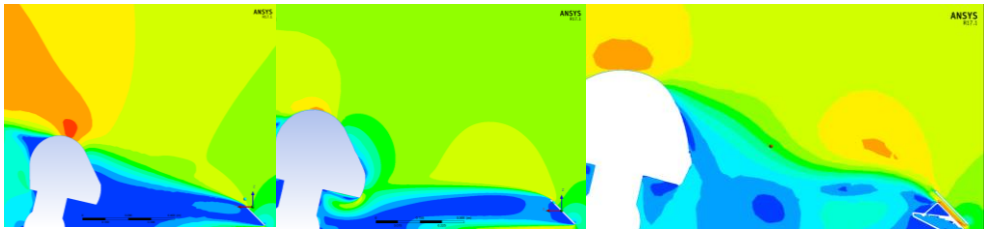

Figure 5.9 Instantaneous steady-state velocity contours for the short windshield for two-dimensionsal (left), partial three-dimensional (center), and full three-dimensional (right) models.

The pressure contours on the rider's helmet also show the differences between the three windshield heights in the full three-dimensional model (Figure 5.10). The contour shows a vertically spread-out high pressure region with the short windshield. The mid windshield height shows a pressure concentration on the forehead, and the tall windshield shows a minimal high pressure area, indicating that the shear layer does not significantly interact with the helmet.

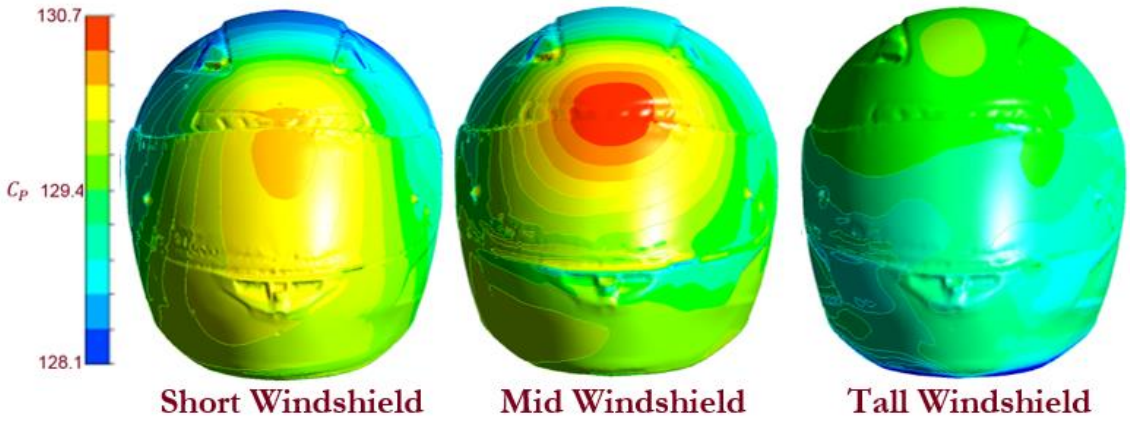

Figure 5.10 Instantaneous steady-state pressure contours on the rider's helmet for short (left), mid (center), and tall (right) windshields in the full three-dimensional model

While solving the steady-state model, the pressure taps located in the helmet were monitored. The locations of these taps are shown as they are located on the test helmet again in Figure 5.11 for reference.

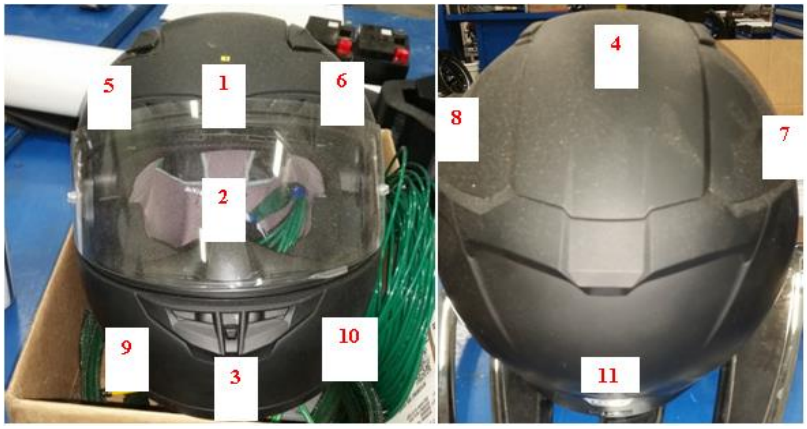

Figure 5.11 Locations of the pressure taps described in Chapter 2

Since the CFX solver uses a false transient and pseudo-time steps as it attempts to iterate to convergence in the steady-state model, these pressure tap monitors can be plotted over time to see if there is any periodic pressure fluctuation. The results of these monitors are shown in Figure 5.12. Clearly, fluctuations exist, but without periodicity.

The plots for the different pressure taps show that convergence to a steady state or a periodic steady state was not achieved. The frequency of the fluctuations at each tap is roughly the same, but amplitude and offset vary, depending on the pressure tap location. The short windshield results show a positive pressure offset for both the forehead and visor pressure taps (one and two), with the other taps all have a negative offset. The results for the mid windshield show that only the forehead (tap one) has a positive pressure offset. The amplitude and frequency of the fluctuations also vary considerably between short and mid windshields.

The frequency associated with the short windshield is 16 Hz, while the frequency associated with the mid height windshield is 12 Hz. The maximum amplitude associated with the short windshield is six times higher than the tall windshield (tap 2), whereas the max amplitude associated with the mid windshield is four times higher than the tall windshield (tap 2). The tall windshield results show fluctuations within the noise of the solution for all taps except those near the top and rear of the helmet (4, 7, 8, and 11). The highest amplitude is at tap 4.

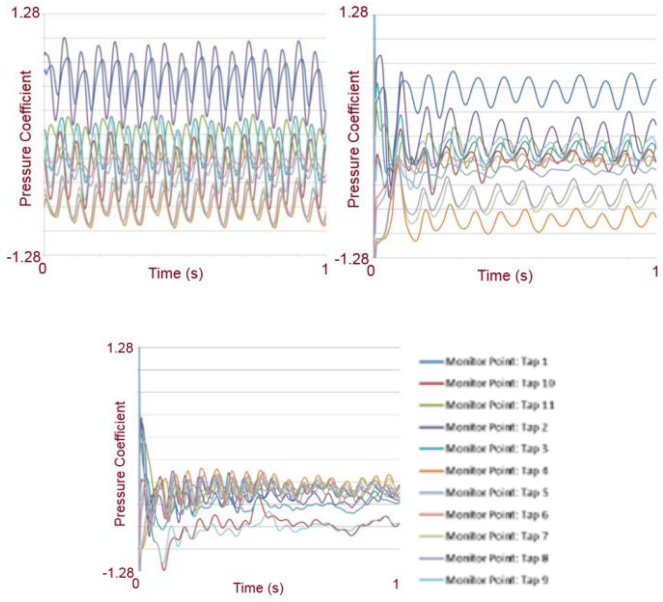

Figure 5.12 Instantaneous pressure tap results for a steady-state full three dimensional model on the helmet for the short (top left), mid (top right), and tall (bottom) windshields. A true steady-state was not achieved

Another quantity that could be tracked in the false transient model was the instantaneous aerodynamic force in each direction on the rider's helmet. The forces calculated by the software include all of the forces normal to the surface of the helmet (pressure forces) and tangential to the surface of the helmet (shear forces). Because the forces are the local pressure forces integrated over the full surface of the helmet, they should fluctuate in the same way as do the pressure tap values.

Figure 5.13 shows the results of the instantaneous false transient forces in each direction for the three windshields investigated. The frequency of fluctuation is the same at it was at the pressure taps. Both the force amplitude and offset are reflective of the false transient solution model. Though the x-direction force has the highest offset relative to its average, all directions appear to fluctuate to some degree. Force fluctuations are high in both x and z directions, while the y-direction has the lowest fluctuation offset. The forces for both the mid and short windshields are consistently in the positive x and z-directions which are downstream and upward respectively. This is to be expected with the shorter windshields due to the direct impingement of the shear layer on the helmet. In the case of the tall windshield though, the x-direction force is negative, while the z-direction force remains upward. These differences affect the degree of discomfort sustained by riders. Though buffeting is much lower with the tall windshield, riders may complain that it feels like someone is pushing their head towards the windshield. The false transient results show that the short windshield will have the worst head buffeting which is in line with what has been found in rider feedback.

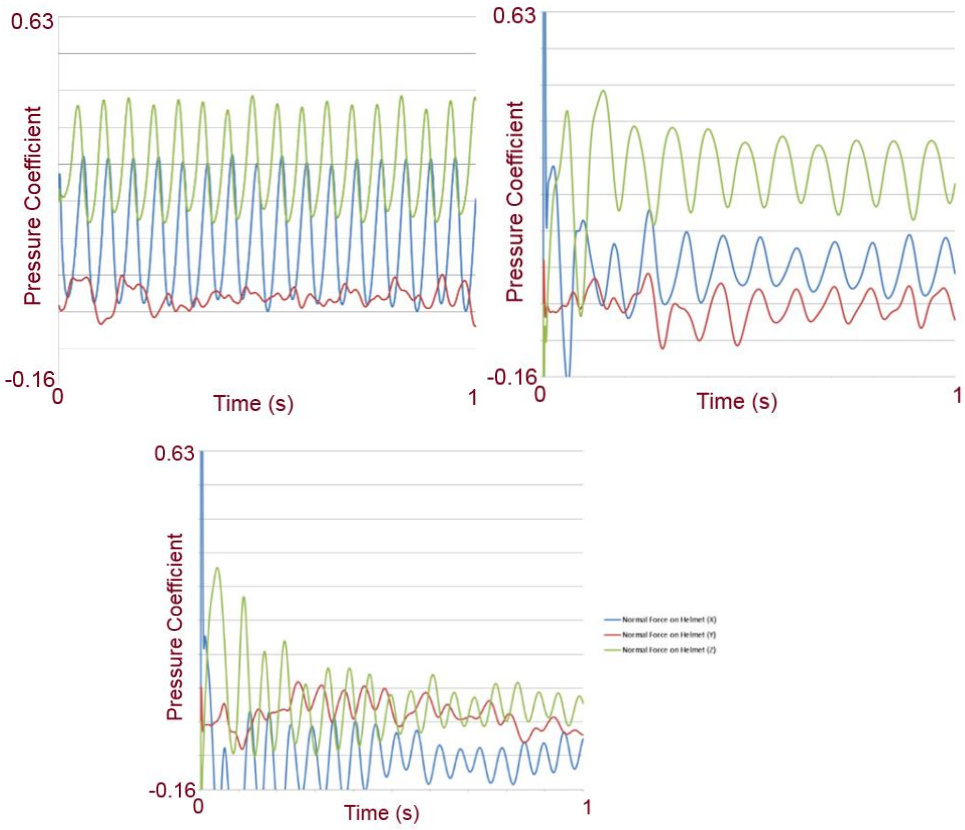

Figure 5.13 Pseudo-transient full three-dimensional helmet force plots for short (top left), mid (top right), and tall (bottom) windshields

5.3.2 True Transient Results

In order to validate the instantaneous steady-state results, a full-transient model was run. This model used the same geometry as the steady-state model but ran as a true transient, initialized from the steady state results. The simulated time for each run was 200 milliseconds, which provided three full periods of fluctuation at the frequencies predicted by the false-transient model. A one millisecond time step was used so that at least 10 time steps occurred in each period. This provided 200 transient results per run. The full transient model was run using the full three-dimensional model.

Figure 5.14 shows the pressure tap results of the transient runs. The average pressure frequency with regard to the short windshield is now 22 Hz. The mid-height

windshield case now has a frequency of 14 Hz on the helmet, and the tall windshield results are mostly flat. The average pressures are similar to those found in the

false-transient case as are the amplitudes of the fluctuations. Qualitatively speaking, the pressure taps appear to behave the same way as they had in the false-transient case. Though the results of the tall windshield case are not fluctuating significantly in the transient case, the average pressure at each location is similar to the results of the false-transient full three-dimensional model. [Please tell us if you are discussing two-d, partial 3-d, or true 3-d results.]

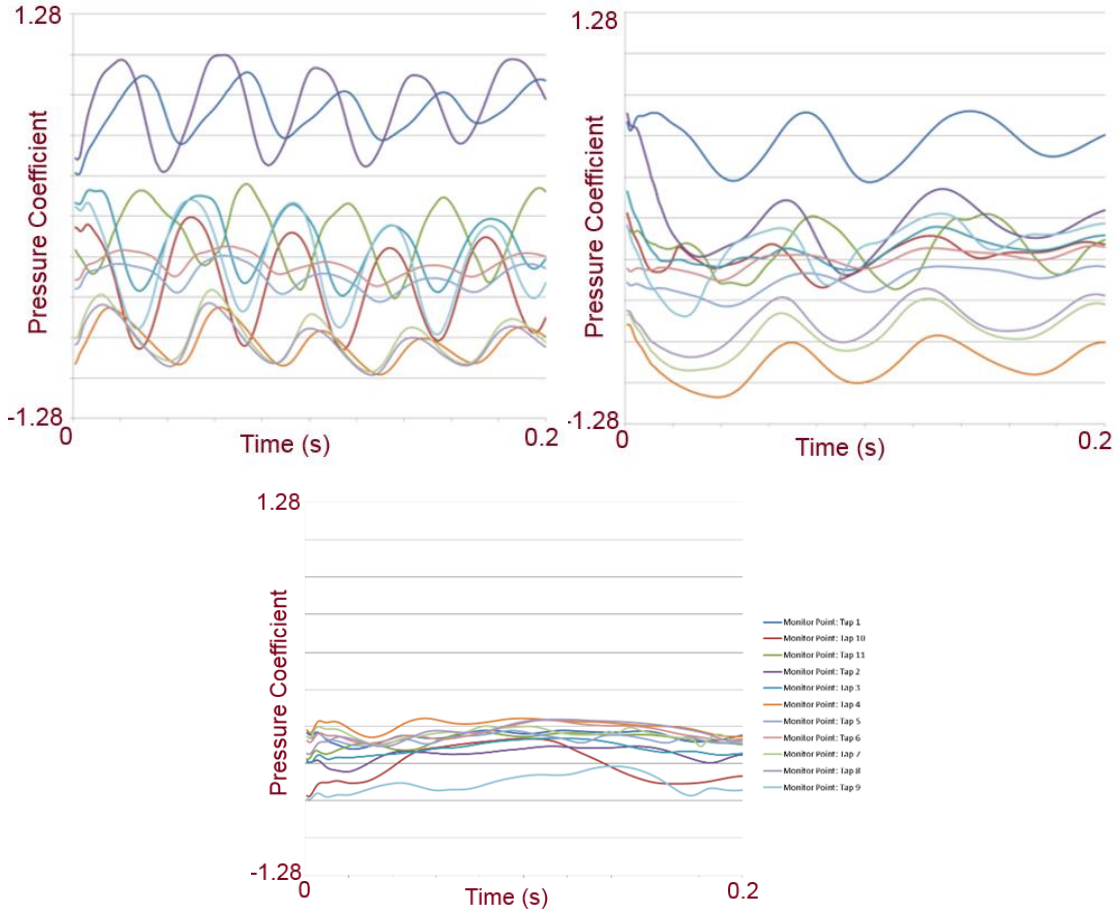

Figure 5.14 True-transient-model full three-dimensional results at pressure taps on the helmet for the short (top left), mid (top right), and tall (bottom) windshields

Figure 5.15 shows the true-transient net directional force values on the rider's helmet. These frequencies are the same as the pressure frequencies, and the time-wise average forces are the approximately the same as what was predicted in the false-transient model. The only windshield that did not perform as expected, when compared to the false-transient results, was the tall windshield, which no longer showed any pressure or force fluctuations.

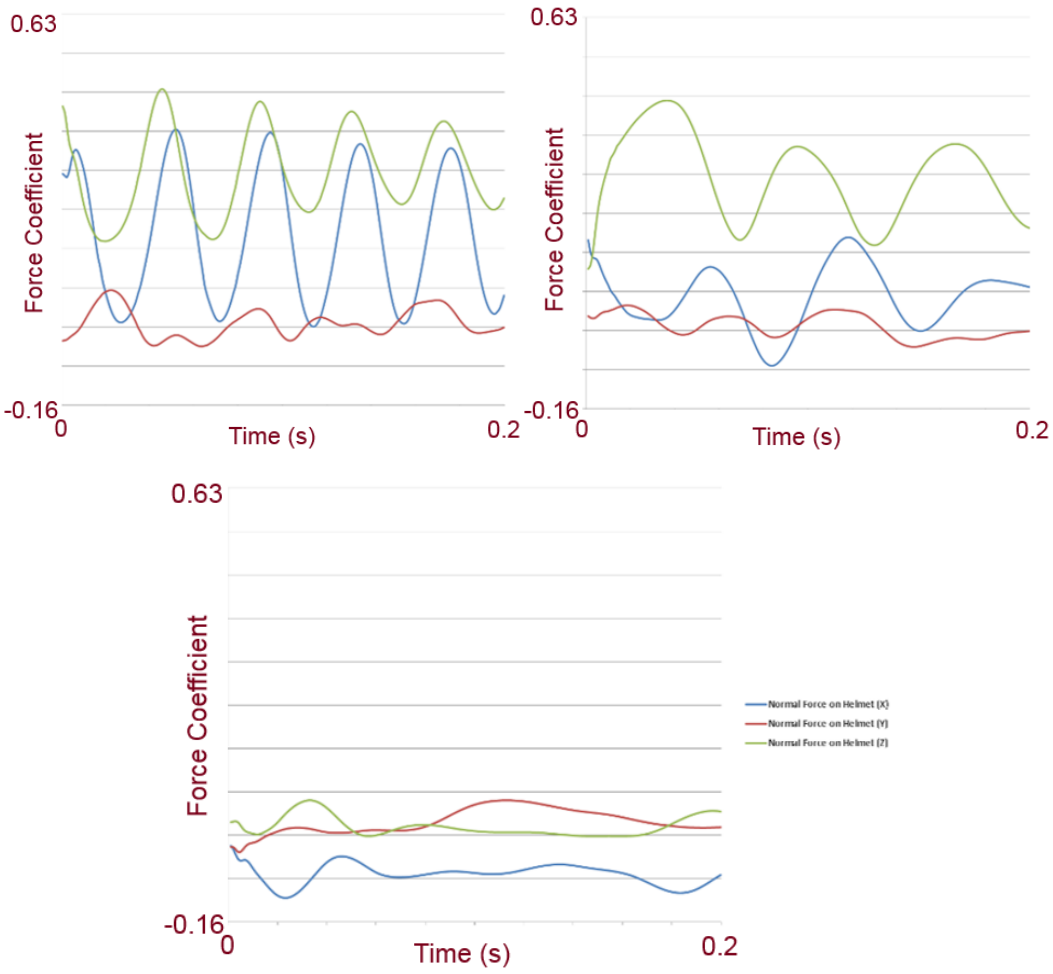

Figure 5.15 True-transient helmet force plots for short (top left), mid (to right), and tall (bottom) windshields

The tall windshield gives rise to the least amount of interaction with the rider's helmet. Because of this, it is likely that the force and pressure fluctuations on the rider's helmet are minimal. The results for the other two windshield heights were in good

agreement with the false-transient model, which gives some confidence to the approach whereby the transient model not being necessary for every analysis.

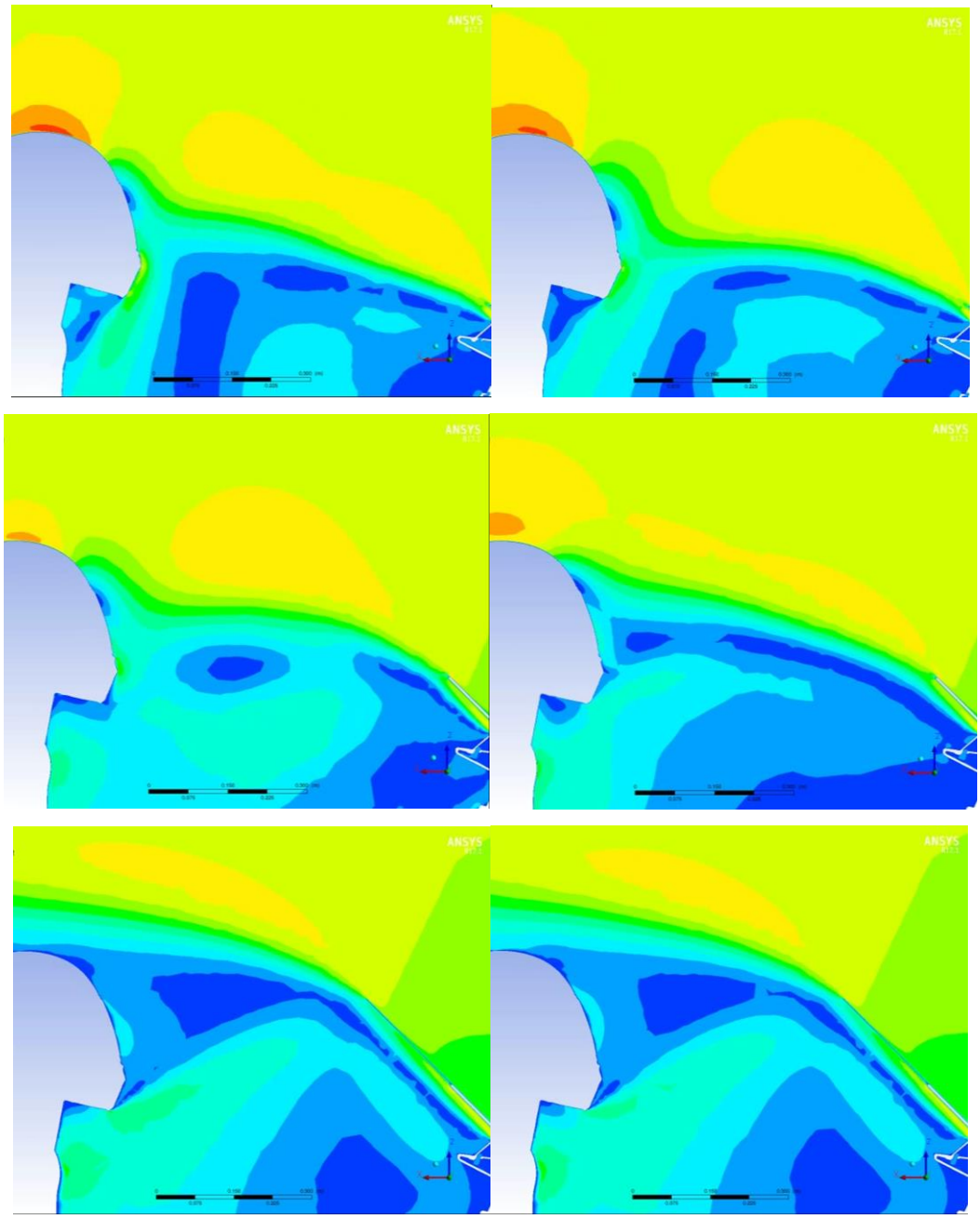

Figure 5.16 Results for two different time steps of the true transient three-dimensional model in the form of center-cut velocity contours for short (top), mid (center), and tall (bottom) windshields

Figure 5.16 shows two frames of the transient velocity contours for each windshield height. The two images of the short windshield show the high velocity vortex moving along the shear layer and then hitting the rider's helmet.

CHAPTER 6

COMPARISON OF EXPERIMENTAL RESULTS WITH NUMERICAL PREDICITONS

This chapter brings together the results determined independently from numerical simulation and experimentation. Computational full-vehicle drag and steady-state static pressure levels will be validated by experiment. Transient simulation models will be validated through comparison of transient smoke data to velocity contours and to pressure fluctuations.

6.1 Drag and Air Resistance

A primary metric for describing the fuel-utilization efficiency of the geometric design of vehicles such as automobiles, motorcycles, and other propelled machines is the drag coefficient. In a certain sense, the magnitude of the drag coefficient is often a critical factor in the acceptance or rejection of a given design. In general, drag consists of two components. One of these, called friction drag, is the result of the frictional interaction between a moving object and a fluid. The other component is called form drag or pressure drag. This component results from the nature of the flow field that envelopes the object in such a way that there is a pressure difference between the forward and rear faces of the object. In this context, the word *form* relates to the shape of the object which is responsible for the pressure difference.

The means by which the drag coefficient is determined in a wind-tunnel setting is mimicked by the approach used to determine this force in the simulation setting. In the former, the wheels of the stationary object are attached to a dynamometer. In the latter, the software calculates the forces, both pressure and shear, on each surface of the object and then sums the separate forces. The forces can then be reduced to a dimensionless

quantity called the drag coefficient for easy comparison between simulation and experiment.

The drag coefficient values calculated from the force transducer in the wind tunnel are compared to those calculated from the false-transient full three dimensional model in CFD in Table 6.1. All CFD computations predicted lower drag coefficients than those of the wind tunnel with the mid windshield showing the largest difference. This outcome is likely due to the idealizing of the rider in the CFD model. There, the rider is considered a rigid, smooth body while, in the wind tunnel, the rider is wearing loose clothing. This also explains why the tall windshield has the lowest deviation of the three, since there is less air moving over the rider. Overall, the agreement between the simulation predictions and the experimental data is satisfactory and sufficient for accepting simulation as a modality for design.

Table 6.1 Drag coefficients for three windshield heights $C_D = \frac{F_D}{\frac{1}{2}\rho V^2 A_{proj}}$

Drag Coefficient	No Windshield	Short Windshield	Mid Windshield	Tall Windshield
Simulation	0.46	0.61	0.63	0.78
Wind Tunnel	0.51	0.67	0.75	0.80
% Difference	9%	9%	18%	2%

6.2 Time-Averaged Pressure Readings

Though the measured pressure fluctuations are of most interest in determining levels of head buffeting, the time-average, static gauge pressure could also be calculated from the data taken on the test track and in wind tunnel. These experimentally determined time-averaged pressure levels were mapped onto the computationally modeled helmet so that they could be compared to the computationally predicted pressure contours. Figure 6.1 shows the values measured in the wind tunnel in their corresponding location on the computational model. For this comparison, high speed was chosen as it provided the highest pressure gradients.

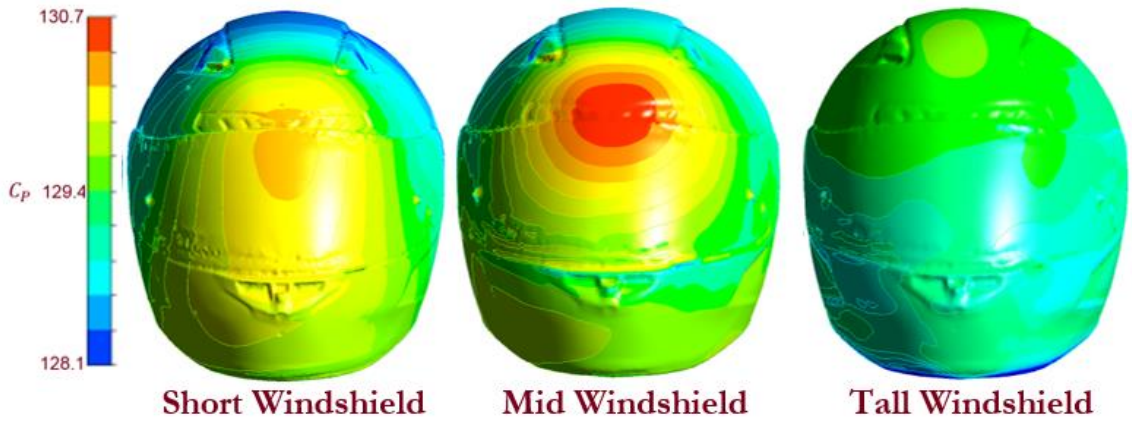

Figure 6.1 Instantaneous steady-state pressure contours on the rider's helmet for short (left), mid (center), and tall (right) windshields in the full three-dimensional model

The computationally determined pressure contours show qualitative agreement with the measured time-averaged pressure tap data, but some of the locations are off considerably. This is due, in part, to the fact that the simulation models never reached a steady-state solution. Table 6.2 shows the tap comparison between analysis and CFD using a time average of the quasi-static results presented in Chapter 5 These results show much better agreement for all the windshields.

Table 6.2 Comparison between average pressures predicted by the stead state full three-dimensional CFD vs wind tunnel data. Pressure values are in terms of the pressure coefficient

Windshield	Tap 1	Tap 2	Tap 3	Tap 4	Tap 5	Tap 6	Tap 7	Tap 8	Tap 9	Tap 10	Tap 11
Short Test	130.2	130.3	129.3	128.8	129.2	129.1	128.8	128.7	129.0	129.2	129.4
Short CFD	130.2	130.2	129.5	128.9	129.3	129.4	128.9	128.9	129.4	129.3	129.6
Mid Test	130.2	130.2	129.4	128.8	129.2	129.2	128.9	128.8	129.2	129.3	129.5
Mid CFD	130.1	129.7	129.5	128.8	129.3	129.4	129.0	129.1	129.5	129.4	129.5
Tall Test	129.2	129.1	129.1	129.2	129.2	129.2	129.2	129.2	129.2	129.2	129.3
Tall CFD	129.3	129.2	129.1	129.4	129.3	129.3	129.3	129.3	128.9	128.9	129.3

Though many of the pressure tap readings are reasonably close to the simulation predictions, a couple measurements are off considerably. The reading of pressure tap two for the mid windshield height is very different than the CFD predicted value. This can be due to the variance of the helmet height between test and CFD. Since this in a very sharp

gradient zone, being off by a few millimeters up or down (relative to the windshield) can be enough to account for this change. Taps nine and ten also appear to be off considerably. This could have to do with the helmet orientation impacting flow along the helmet.

6.3 Transient Pressure Readings

A comparison of the pseudo-transient results from CFD to the pressure tap readings measured in the wind tunnel is set forth in Figures 6.2-6.7. Among these, Figures 6.2 and 6.3 are for the short windshield, 6.4 and 6.5 are for the intermediate height, and 6.6 and 6.7 are for the tallest windshield. In each figure, the pressure fluctuations are plotted as a function of time over a one-second interval following the termination of the startup transient.

It can be seen that the computational results contain less frequency content than do the test data, though the general characteristics are similar between the two. Qualitatively, the tap locations at which high pressure values are encountered are the same for both experiment and simulation. The frequencies seen in the CFD traces also appear in the test data. The CFD does not capture all of the experimental information though, as the higher frequencies (above 20 Hz) are completely neglected in the computational results.

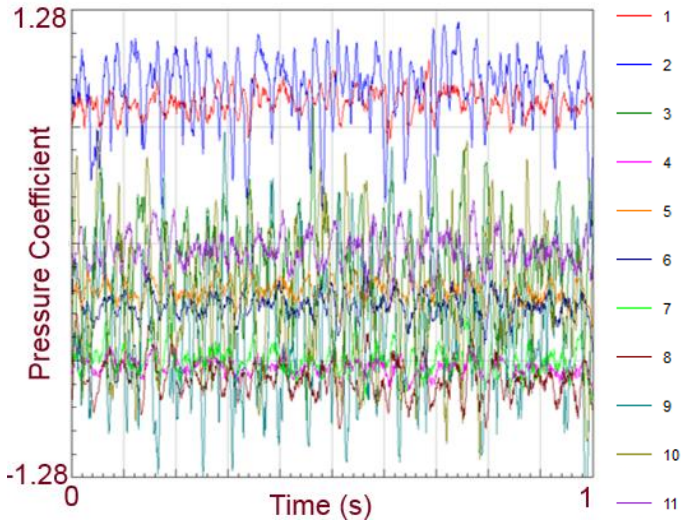

Figure 6.2 Pressure tap fluctuations over a one-second time interval for the short windshield in the wind tunnel

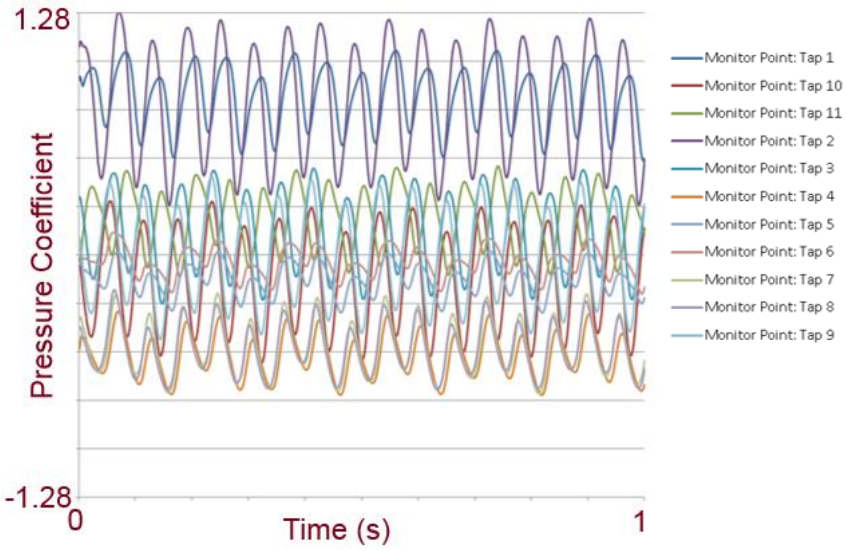

Figure 6.3 Pressure tap fluctuations over a one-second time interval for the short windshield in CFD

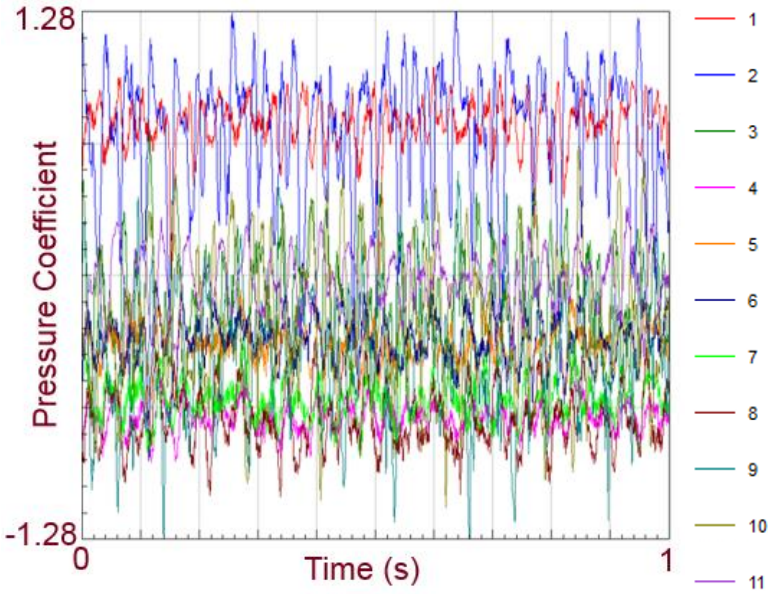

Figure 6.4 Pressure tap fluctuations over a one-second time interval for the mid-height windshield in the wind tunnel

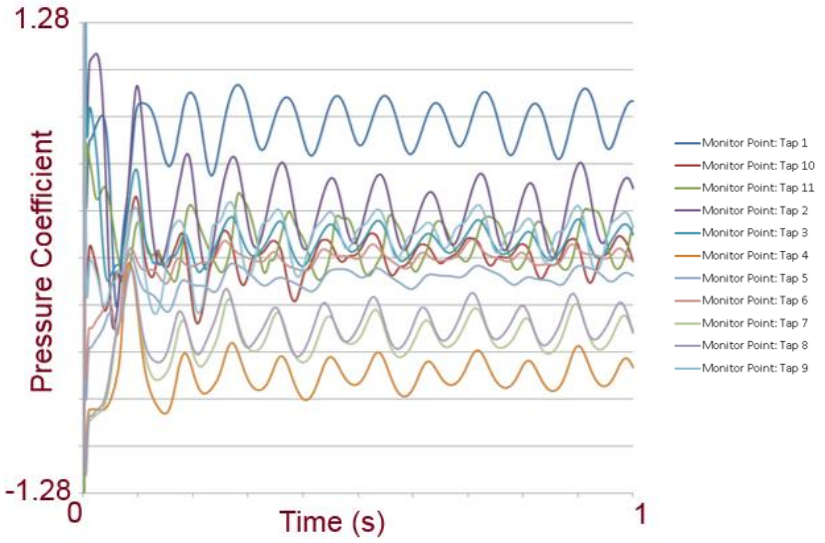

Figure 6.5 Pressure tap fluctuations over a one-second time interval for the mid-height windshield in CFD

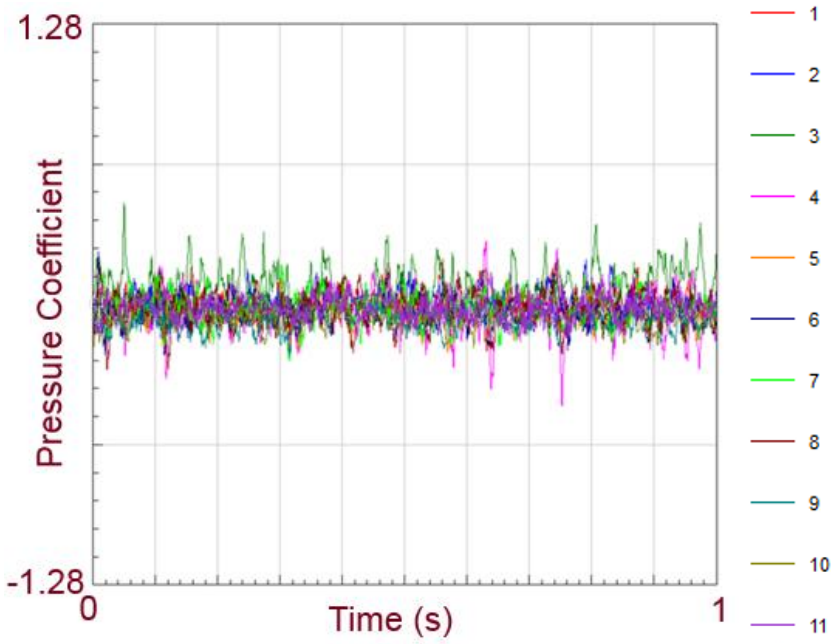

Figure 6.6 Pressure tap fluctuations over a one-second time interval for the tall windshield in the wind tunnel

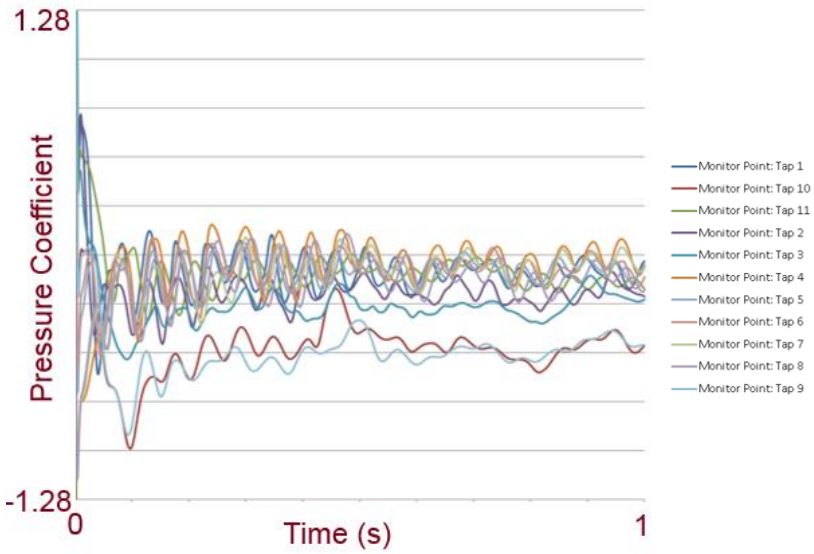

Figure 6.7 Pressure tap fluctuations over a one second-time interval for the tall windshield in CFD

One of the chief consequences of the frequency differences between testing and analysis is on side-to-side head movement. While analysis predicts that there will be minimal side-to-side movement, the test data strongly suggest that there is forcing in that direction. Inspecting the pressure taps that have a side-to-side component reveals that, in the computational case, opposite pressure taps are in phase with each other resulting in a net side force of zero (Figure 6.8). On the other hand, the test data shows the pressure fluctuations on either side of the helmet are out of phase with each other, thus having an additive effect on side-to-side helmet forcing.

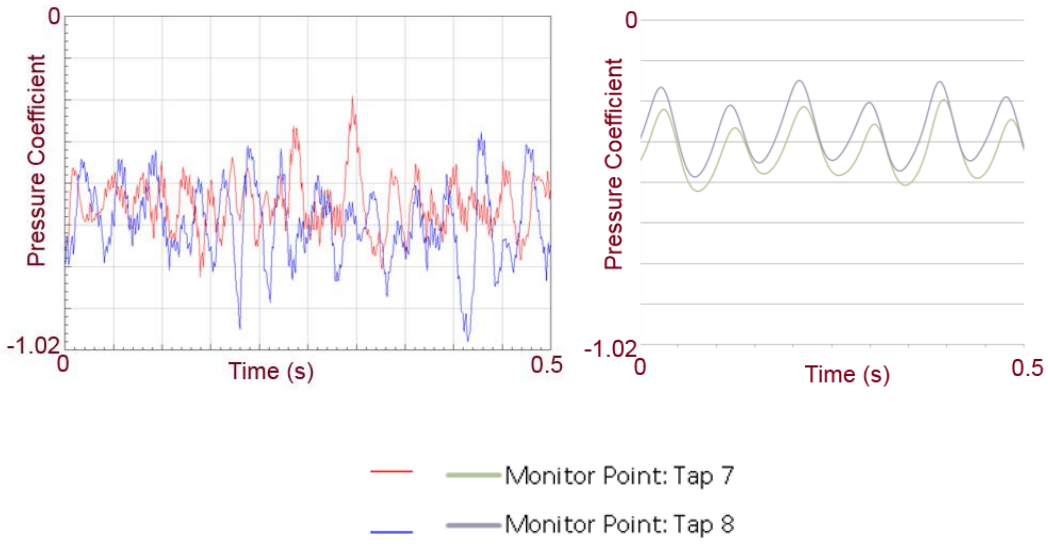

Figure 6.8 showing pressure taps 7 and 8 for test (left) and CFD (right)

One of the likely reasons for this discrepancy is the simplification of the CFD model to neglect fluid-structural interactions between the fluid, rider, and flexible motorcycle components. The windshields and other motorcycle bodywork likely have a fluttering effect and impact buffeting frequencies. The reaction forces of the head are complicated and likely impact head buffeting patterns on the helmet.

Lastly, it is very difficult for a rider to remain in a fixed position on the motorcycle like the manikin does in the CFD model. The aerodynamic loading on the rider impacts the helmet position relative to the fairing. Rider fatigue and discomfort can cause shifting in position during the test. Rider size, shape, and clothing are also known to impact head buffeting.

CHAPTER 7

ACOMPLISHMENTS

The primary motivation for the research of this thesis is to relate motorcycle aerodynamics to the physiological outcomes of the aerodynamic forces on the rider. The strength of the research is reinforced by the utilization of a synergistic combination of numerical simulation and experimentation. A special focus of the research is the impact of the position of the motorcycle windshield on the motorcycle and the resulting forces that are sustained by the rider,

The background for the experiments is set forth in Chapter 2. There, the distinction between a wind-tunnel test environment and an outdoor test track is sharply drawn. In truth, the less-controlled test-track environment argued against extensive experiment there. As a consequence, the wind tunnel results served as the main counterpart to those of the numerical simulation. In Chapter 2, a painstaking methodology for using information from 11 individual pressure taps, situated on the helmet of the rider, was developed to provide net forces in each of three coordinate directions. To compliment the determination of the forces as just described, the accelerations experienced by an accelerometer probe were identified. These components of Newton's second law were brought together in Chapter 3. There, it was found that the matching of the change in momentum with the net force was fulfilled to a high degree of excellence. This outcome lends strong support to the experimental conception, implementation, and data extraction.

A sharp focus on the unsteady nature of the fluctuations experienced by the rider is made in Chapter 3 where the experimental results for the frequency of the fluctuations are featured graphically from wind tunnel runs. Separate presentation is made of the fluctuations at the helmet pressure taps and those experienced by the accelerometer. In general, the fluctuations experienced at the tap sites extended over a broader range of frequencies than did those at the accelerometer. A critical parameter, with regard to both

the frequency range and magnitude, is the height of the windshield. The fluctuations of greatest magnitude were those which occurred when the windshield was in its lowest position. At the highest position of the shield, the fluctuation magnitudes were least. This finding serves as a guide for motorcycle rider positioning with respect to the windshield to minimize undesired physiological effects. In general, it may be concluded that for rider comfort and safety, the windshield position should be at its maximum height or there should be no windshield at all.

The wind tunnel experiments also made use of smoke-based flow visualization to enable examination of the path of air flow imposed by the windshield. It was clearly seen that, at the lowest windshield setting, the smoke path impinged directly on the rider's chin and lower portion of the face. On the contrary, a high windshield setting gave rise to a smoke trail that lofted above the rider's forehead.

The test track results were, necessarily, more limited than those from the wind tunnel studies. Comparisons of the results from the two test sites included fluctuations at the pressure taps and at the accelerometer. In general, satisfactory qualitative agreement occurred from the comparison. However, not unexpectedly, there were deviations which could be attributed to the uncontrolled environmental situation in the neighborhood of the test track.

To achieve the desired synergy between experiment and prediction, a suite of numerical simulations was performed. This suite consisted of: (a) a spatially two-dimensional model, (b) a partially three-dimensional model, and (c) a full three-dimensional model. Among these, (a) and (c) were implemented both for steady state and unsteady operating conditions. For the (b) approach, only a steady solution was obtained. The latter strategy was based on the initial finding that the steady-state solution did not reveal sufficient information to encourage extension of that work beyond steady state.

The solution domain for the two-dimensional model did not extend laterally to the sides of the machine. It did, however, extend both fore and after. In contrast, the three-dimensional model enhanced the solution domain by virtue of substantial lateral

extensions to both sides of the machine. The three-dimensional, unsteady solutions were extremely time consuming and continued fluctuating indefinitely, but showed a tendency toward periodicity at large times.

Due to the larger blockage caused by the tall windshield, the predicted airflow pattern is more accelerated coming off of the windshield, but it almost completely misses the rider's helmet. This suggests that buffeting would be minimal with the use of the tall windshield. The short windshield, on the other hand, produces a smaller airspeed coming off of the windshield, but the shear layer directly impinges on the rider's head. This suggests the head buffeting would be a concern with this windshield. Another interesting characteristic of the short windshield model is that the maximum velocity is located above and behind the rider's helmet.

The predicted pressure contours on the rider's helmet also show the differences between the three windshield heights. The contour diagrams show a vertically spread-out high pressure region with the short windshield. The mid windshield shows a pressure concentration on the forehead, and the tall windshield shows a minimal high pressure area, indicating that the shear layer does not significantly interact with the helmet. The predicted fluctuation frequencies from the full three-dimensional and full transient model indicate a definitive gradation as a function of the windshield height. The highest frequencies correspond to the shortest windshield, with a significant diminution in frequency at the mid-height, and virtually no fluctuations at full height.

Among the global outcomes of this study, the drag force experienced by the machine is of great importance since it serves as a metric for the quality of the design. Values of the drag force were obtained from the wind tunnel experiments and independently from the numerical simulations. The means by which the drag force is determined in a wind tunnel setting is mimicked by the approach used to determine this force in the simulation setting. In the former, the wheels of the stationary object are attached to a dynamometer. In the latter, the software calculates the forces, both pressure and shear, on each surface of the object and then sums the separate forces.

The drag results predicted by all of the simulation models were found to be lower than the drag from the wind tunnel but still satisfactory. The difference is likely due to the idealizing of the rider in the CFD model. There, the rider is considered a rigid, smooth body while, in the wind tunnel, the rider is wearing loose clothing. This also explains why the tall windshield has the lowest deviations of the three, since there is less air moving over the rider. Overall, the agreement between the simulation predictions and the experimental data are satisfactory and sufficient for accepting simulation as a modality for design.

The predicted helmet pressure contours show satisfactory qualitative agreement with the measured pressure tap, time-averaged values, reinforcing the simulation model. This outcome demonstrates the wisdom of the two-prong approach used here, whereby experimentation and simulation are both employed independently. Being able to employ both approaches may be somewhat of a luxury in the context of a busy industrial environment. In that light, the present results have a special significance in that they demonstrate the positive interaction of the two approaches. From that standpoint alone, the value of the present investigation has been well proven.

Another unique value of the work performed here is the quantification of the pressure buffeting of the rider as measured by means of pressure taps and accelerometer recordings. Moreover, the correlation between pressure tap characteristics and those of the accelerometer has never before been attempted. The excellence of the correlation achieved here, as witnessed by Newton's Second Law, suggests that future work need not involve separate pressure tap and accelerometer measurements.

A less quantitative but still useful measurement technique was used effectively here and demonstrated to have utility. The technique is a qualitative assessment of the sensations experienced by the rider. This assessment was brought together with the quantitative metrics and shown to be well within the range of outcomes from the metrics measurements. This provides a physiological relation to the quantitative measurements.

References

[1] Biancolini, M. E., et al. "Industrial application of the meshless morpher RBF morph to a motorbike windshield optimization." Simulation for Innovative Design: Proceedings of the 4th European Automotive Simulation Conference. 2009.

[2] Takahashi, Yasushi, et al. CFD Analysis of Airflow around the Rider of a Motorcycle for Rider Comfort Improvement. No. 2009-01-1155. SAE Technical Paper, 2009.

[3] Angeletti, Mario, et al. The role of CFD on the aerodynamic investigation of motorcycles. No. 2003-01-0997. SAE Technical Paper, 2003.

[4] Bella, Gino, Stefano Ubertini, and Umberto Desideri. Experimental and Computational Analysis of the Aerodynamic Performances of a Maxi-Scooter. No. 2003-01-0998. SAE Technical Paper, 2003.

[5] Shimizu, Tohru, et al. Simultaneous Evaluation on Aerodynamics and Air-cooling Performances for Motorcycle using CFD Analysis. No. 2009-32-0138. SAE Technical Paper, 2009.

[6] Kennedy, John, et al. "The effects of windscreen flow on noise in motorcycle helmets." Proceedings of Meetings on Acoustics. Vol. 12. No. 1. Acoustical Society of America, 2014.

[7] Garcia, Nelson, Hector Arocha, and Jose Lorenzo. Aerodynamic Study of Prototype Motorcycle Using Experimental Techniques and Visualization Flow. No. 2005-01-3993. SAE Technical Paper, 2005.

[8] Tempia, Angelo, and Riccardo Pagliarella. "A Preliminary Investigation into Racing Motorcycle Aerodynamics." The Engineering of Sport 6. Springer New York, 2006. 139-144.

[9] Bella, G., et al. Application of an Integrated CFD Methodology for the Aerodynamic and Thermal Management Design of a Hi-Performance Motorcycle. No. 2013-24-0143. SAE Technical Paper, 2013.

[10] Carley, Michael, et al. "The experimental measurement of motorcycle noise."Proceedings of Meetings on Acoustics. Vol. 12. No. 1. Acoustical Society of America, 2014.

[11] Lower, M. C., D. W. Hurst, and A. Thomas. "Noise levels and noise reduction under motorcycle helmets." PROCEEDINGS-INSTITUTE OF ACOUSTICS 18 (1996): 979-982.

[12] Kennedy, J., et al. "On-road and wind-tunnel measurement of motorcycle helmet noise." The Journal of the Acoustical Society of America 134.3 (2013): 2004-2010.

[13] McCombe, Andrew W., J. A. Binnington, and D. Nash. "Wind noise and motorcycle crash helmets." Journal of low frequency noise & vibration 13.2 (1994): 49-57.

[14] Araki, Yuji, and Kazuhiro Gotou. Development of aerodynamic characteristics for motorcycles using scale model wind tunnel. No. 2001-01-1851. SAE Technical Paper, 2001.

[15] Desai, Sachin, et al. Experimental and CFD Comparative Case Studies of Aerodynamics of Race Car Wings, Underbodies with Wheels, and Motorcycle Flows. No. 2008-01-2997. SAE Technical Paper, 2008.

[16] Akaike, S., et al. "Study of noise reduction of automotive cooling fans." ASME PRESSURE VESSELS PIPING DIV PUBL PVP, ASME, NEW YORK, NY(USA), 1992, 243 (1992): 15-25.

[17]Coffen, Charles D., et al. "Transferring Aerospace Technology to Commercial Products: Aeroacoustic Prediction Methods for Automobile Radiator Fans."ASME-PUBLICATIONS-FED 219 (1995): 77-82.

[18] Magne, Stéphan, et al. "Aeroacoustic prediction of an automotive cooling fan." Canadian Acoustics 39.3 (2011): 32-33.

[19] Wickern, Gerhard, and Martin Brennberger. “Helmholtz Resonators Acting as Sound Source in Automotive Aeroacoustics.” No. 2009-01-0183. SAE Technical Paper, 2009.

[20]Cespón, José Luis González, et al. "Characterization of the Attenuation Properties in Motorcycle Helmets." Acta Acustica united with Acustica 99.6 (2013): 1008-1013.

[21] Duell, Edward G., et al. “Progress in Aeroacoustic and Climatic Wind Tunnels for Automotive Wind Noise and Acoustic Testing.” No. 2013-01-1352. SAE Technical Paper, 2013.

[22]Menter, F. R., M. Kuntz, and R. Langtry. "Ten years of industrial experience with the SST turbulence model." Turbulence, heat and mass transfer 4.1 (2003): 625-632.

[23] Li, A., Chen, X., Chen, L., & Gao, R. (2014, April). “Study on local drag reduction effects of wedge-shaped components in elbow and T-junction close-coupled pipes.” In Building Simulation (Vol. 7, No. 2, pp. 175-184). Tsinghua University Press.

[24] W. Li, J. Ren, J. Hongde, Y. Luan, P. Ligrani, “Assessment of six turbulence models for modeling and predicting narrow passage flows, Part 2: Pin fin arrays.” Numer. Heat Tr. A-Appl., vol. 69, pp. 445-463, 2016.

[25] U. Engdar and J. Klingmann, “Investigation of Two-Equation Turbulence Models Applied to a Confined Axis-Symmetric Swirling Flow.” In ASME 2002 Pressure Vessels and Piping Conference, pp. 199-206, 2002.

[26] Park, J., Park, S., & Ligrani, P. M. (2015). “Numerical predictions of detailed flow structural characteristics in a channel with angled rib turbulators.” Journal of Mechanical Science and Technology, 29(11), 4981-4991.

[27] E.M. Sparrow, J.M. Gorman, and J.P. Abraham, “Quantitative Assessment of the Overall Heat Transfer Coefficient U.” ASME Journal of Heat Transfer, vol. 135, p. 061102, 2013.

[28] Y. Bayazit, E.M. Sparrow, and D.D. Joseph, “Perforated Plates for Fluid Management: Plate Geometry Effects and Flow Regimes.” International Journal of Thermal Sciences, vol. 85, pp. 104-111, 2014.

[29] P. D. Clausen, S. G. Koh, and D. H. Wood, “Measurements of a swirling turbulent boundary layer developing in a conical diffuser.” Exp. Therm. Fluid Sci., vol. 6, pp. 39-48, 1993.

[30] J.M. Gorman , E.M. Sparrow J.P. Abraham , W.J. Minkowycz, “Evaluation of the efficacy of turbulence models for swirling flows and effect of turbulence intensity on heat transfer.” Numer. Heat Tr. B-Fund., (Accepted).